Cell Reports

Article

Single-cell transcriptomics of human-skin-equivalent organoids

Graphical abstract

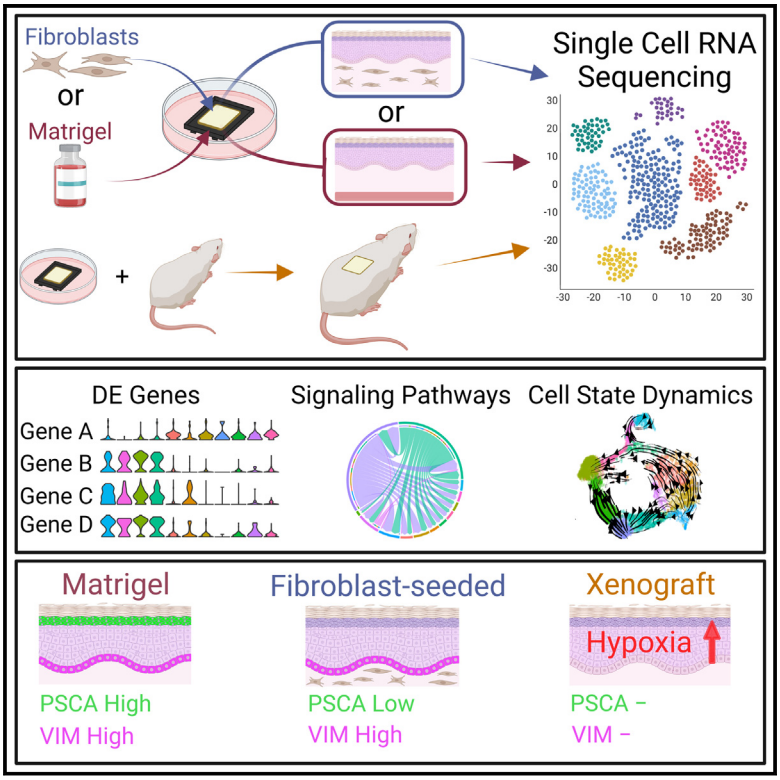

Highlights

- Human-skin-equivalent organoids retain *in vivo* cellular states
- Culture conditions can alter existing molecular programs and induce aberrant EMT-like states
- Xenografting organoids or hypoxic culturing can rescue some aberrant signaling programs

Authors

Adam R. Stabell, Grace E. Lee, Yunlong Jia, ..., George L. Sen, Qing Nie, Scott X. Atwood

Correspondence

satwood@uci.edu

In brief

Stabell et al. use single-cell transcriptomics to define the similarities and differences between *in vivo* human epidermis and human-skin-equivalent organoids. Some aberrant culture-specific differentiation or progenitor signaling programs can be rescued upon xenografting or culturing organoids under hypoxic conditions.

Stabell et al., 2023, Cell Reports *42*, 112511
May 30, 2023
https://doi.org/10.1016/j.celrep.2023.112511

CellPress

Cell Reports

CellPress
OPEN ACCESS

Article

Single-cell transcriptomics of human-skin-equivalent organoids

Adam R. Stabell,[1,2] Grace E. Lee,[1] Yunlong Jia,[1] Kirsten N. Wong,[1,2] Shuxiong Wang,[3] Ji Ling,[4] Sandrine D. Nguyen,[1] George L. Sen,[4,5] Qing Nie,[1,2,3,6] and Scott X. Atwood[1,2,6,7,8,*]

[1]Department of Developmental and Cell Biology, University of California, Irvine, Irvine, CA 92697, USA
[2]NSF-Simons Center for Multiscale Cell Fate Research, University of California, Irvine, Irvine, CA 92697, USA
[3]Department of Mathematics, University of California, Irvine, Irvine, CA 92697, USA
[4]Department of Dermatology, University of California, San Diego, La Jolla, CA 92093, USA
[5]Department of Cellular and Molecular Medicine, UCSD Stem Cell Program, University of California, San Diego, La Jolla, CA 92093, USA
[6]Center for Complex Biological Systems, Chao Family Comprehensive Cancer Center, University of California, Irvine, Irvine, CA 92697, USA
[7]Department of Dermatology, University of California, Irvine, Irvine, CA 92697, USA
[8]Lead contact
*Correspondence: satwood@uci.edu
https://doi.org/10.1016/j.celrep.2023.112511

SUMMARY

Several methods for generating human-skin-equivalent (HSE) organoid cultures are in use to study skin biology; however, few studies thoroughly characterize these systems. To fill this gap, we use single-cell transcriptomics to compare *in vitro* HSEs, xenograft HSEs, and *in vivo* epidermis. By combining differential gene expression, pseudotime analyses, and spatial localization, we reconstruct HSE keratinocyte differentiation trajectories that recapitulate known *in vivo* epidermal differentiation pathways and show that HSEs contain major *in vivo* cellular states. However, HSEs also develop unique keratinocyte states, an expanded basal stem cell program, and disrupted terminal differentiation. Cell-cell communication modeling shows aberrant epithelial-to-mesenchymal transition (EMT)-associated signaling pathways that alter upon epidermal growth factor (EGF) supplementation. Last, xenograft HSEs at early time points post transplantation significantly rescue many *in vitro* deficits while undergoing a hypoxic response that drives an alternative differentiation lineage. This study highlights the strengths and limitations of organoid cultures and identifies areas for potential innovation.

INTRODUCTION

Skin is an essential organ with many roles, including forming a water-tight barrier, aiding thermoregulation, and acting as a sensory organ.[1] To fulfill these roles, the keratinocytes that constitute the epidermis must replenish themselves while withstanding a constant barrage of chemical, physical, pathological, and radiological insults from their environment.[2,3] The field of skin research has largely been driven by *in vivo* mouse models that show that healthy skin is critical for an organism's well-being and that disruption of many of its functions can lead to a drastic decline in quality of life.[4,5] While mice are suitable to define the basic architecture and homeostatic signaling of skin, the anatomy, microstructure, and heterogeneity of mouse skin is inherently different from human skin.[1,6] For instance, mice have a distinct density of hair follicles and eccrine glands, a layer of striated muscle found beneath the hypodermis, a lack of melanocytes in the interfollicular epidermis (IFE), and absence of rete ridges. These differences impact epidermal homeostasis, wound repair, and the severity of certain skin disorders, pointing to a need for a more human-equivalent model system to study human-specific aspects of skin biology.[5]

Three-dimensional (3D) organoid cultures have long been a tool to investigate complex tissue interactions.[7,8] Typically composed of primary cells isolated from patient samples, the idea of building an organ from its basic components is an attractive premise that has profound scientific implications.[9] From gaining molecular insight by simplifying development and homeostasis to their essential parameters to the translational promise of a gold-standard system to test drugs or a farm system to grow replacement tissues, 3D organoid cultures are gaining popularity as an elegant and relevant model system to study human biology. Current technologies include generating complex skin in spherical cell aggregates from human pluripotent stem cells,[10,11] using conventional scaffolds, such as hydrogels[12–14] or bioprinting,[11,15,16] to assemble dermal and keratinocyte layers with other relevant cells, and organs-on-a-chip that allow active perfusion and spatiotemporal control at the microscale level.[17]

However, 3D cultures are not without their limitations. For instance, despite human-skin-equivalent (HSE) organoid cultures showing a high degree of morphological similarity to their *in vivo* counterparts, their composition and culture conditions vary greatly from lab to lab, which can affect interpretation of

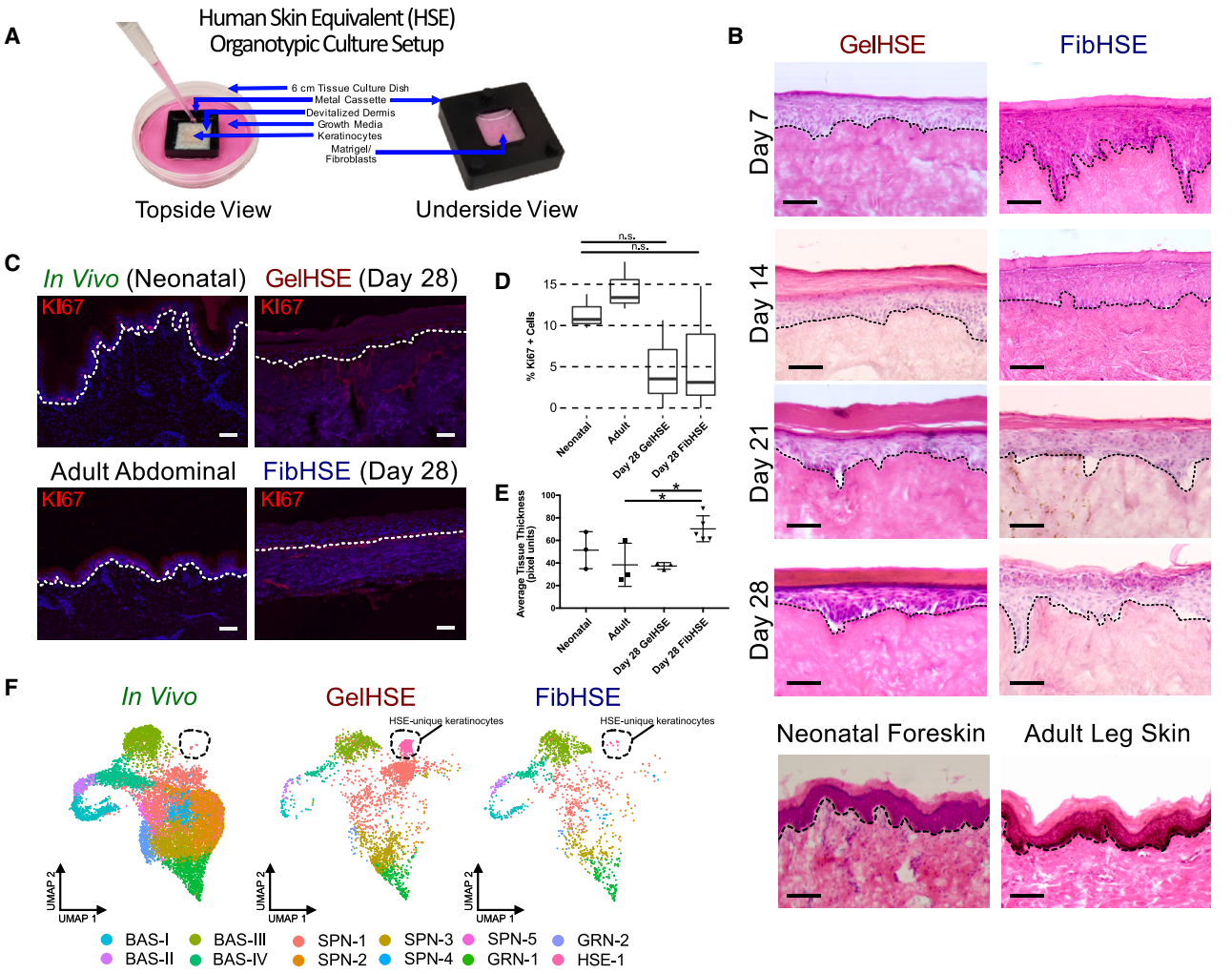

(legend on next page)

similar experiments.[9–11,16,18,19] Many components of the *in vivo* system are lacking, such as vasculature and immune cells, which limits the size of cultures and their response to experimental stimuli.[9] Many studies defining HSEs have shown marked molecular differences in basal and terminal gene expression that suggest that epidermal differentiation is not quite analogous to the *in vivo* counterparts.[20,21] Given the variability that exists between culture systems and their limited characterization, it can be difficult to determine which conditions are best suited for a particular experiment (Figures S1A and S1B). Knowledge of the capacity and limitations of these systems is paramount to accurately interpret results.

Recently, several labs have published single-cell omics studies examining the strengths and weaknesses of a variety of organotypic culture systems. These include organoids mimicking the central nervous system,[22] gastric system,[23] intestinal system,[24] and gastrulation.[25] Human skin spheroids have recently been developed from human pluripotent stem cells that differentiate into spherical cell aggregates where cyst-like skin emerges, composed of stratified epidermis, fat-rich dermis, pigmented hair follicles with sebaceous glands, and rudimentary neural circuitry.[10] Although these skin spheroids resemble fetal facial skin, their long incubation period and small size are not ideal for genetic manipulation of individual cell types or for grafting in the clinic. How HSEs built using conventional scaffolds like devitalized dermis compare with their *in vivo* counterparts is unclear, despite being ideally suited to address the deficiencies of spherical skin organoids.

Our lab, alongside others, has recently shown that human epidermis is more heterogeneous than previously thought.[26–29] Using single-cell RNA sequencing (scRNA-seq) and subsequent *in vivo* validation, we spatially resolved four distinct basal stem cell populations within human IFE and delineated multiple spinous and granular cell populations that contributed to a hierarchical differentiation lineage supporting multi-stem-cell epidermal homeostasis models.[27] Collectively, these studies have highlighted the complexity of the epidermis and its cell-cell interactions. The extent to which HSEs can recapitulate the cell type heterogeneity, cell-cell signaling, and differential gene expression of *in vivo* human skin remains unclear. To address this issue, we probed the transcriptomes of three HSE variants, two *in vitro* HSEs and one xenografted HSE, and examined the differences in comparison with *in vivo* human skin at the single-cell level. We found that all HSEs remarkably contained the relevant cellular states of their *in vivo* counterparts, but each HSE also possessed unique cell states not found during homeostasis. An expanded basal program, terminal differentiation defects, and ectopic epithelial-to-mesenchymal transition (EMT) signatures predominate fibroblast- and Matrigel-derived HSEs, whereas xenografting HSEs onto immunodeficient mice largely rescued the various defects at the cost of inducing hypoxic conditions.

RESULTS

Histological characterization of HSEs

To compare commonly used *in vitro* HSEs with *in vivo* human epidermis, we chose to use devitalized human dermis as the scaffold for growing the HSEs because we reasoned that the extracellular matrix composition more accurately mimics the endogenous surface for keratinocyte stratification than a collagen-based hydrogel. We utilized the two most common HSE variants, where primary human keratinocytes are seeded on top of devitalized dermis at the air-liquid interface, and the dermis is either treated with Matrigel (GelHSEs)[30] or seeded with primary human dermal fibroblasts (FibHSEs)[8] to supply necessary signals for keratinocyte stratification (Figure 1A). Keratinocyte stratification occurs under both conditions by day 7, where the HSEs show a tightly packed columnar basal cell layer, multiple irregular polyhedral squamous cell layers, several flattened granular cell layers, and a thin stratum corneum (Figure 1B). Histologically, the HSEs largely remain the same up through day 28, except for a thickening of the stratum corneum and a general spreading out of keratinocytes at all epidermal layers. Proliferation was reduced in the HSEs over time, and day 28 tissue showed less proliferation compared with neonatal or adult epidermis, with no significant change in apoptosis (Figures 1C, 1D, S1A, and S1B). FibHSEs possess a significantly thicker living epidermal layer than the GelHSEs (Figure 1E). We chose to continue our analysis with day 28 HSEs because of the morphological similarity to *in vivo* tissue and to avoid active re-stratification or injury programs that may be operating at earlier time points.

Epidermal homoeostasis is disrupted in HSEs

To define the cellular states of keratinocytes derived from HSEs, we isolated viable single cells from day 28 HSEs and subjected

Figure 1. Defining HSE cell populations using scRNA-seq

(A) Diagram of the human-skin-equivalent (HSE) organoid culture setup.

(B) Hematoxylin and eosin (H&E) staining of Matrigel-grown HSEs (GelHSEs) and fibroblast-seeded HSEs (FibHSEs) after 7, 14, 21, and 28 days of growth on devitalized human dermis. Neonatal epidermis from foreskin and adult epidermis from the leg are shown for comparison. Scale bars, 100 μm. Dashed lines denote the epidermal-dermal junction.

(C) Immunostaining of KI67 (red) and DAPI (blue) in human neonatal skin (top left), adult abdominal skin (bottom left), day 28 GelHSEs (top right), and day 28 FibHSEs (bottom right). Scale bars, 100 μm. Dashed lines denote the epidermal-dermal junction.

(D and E) Quantification of (D) KI67+ cells and (E) average thickness of living epidermal cell layers in human neonatal skin, adult abdominal skin, day 28 GelHSEs, and day 28 FibHSEs. n = 3 each sample. Significance was determined by Tukey's HSD (honestly significant difference) test. *$p < 0.05$. n.s., not significant. Error bars represent the standard error of the mean (SEM).

(F) Seurat clustering of 15,573 single cells isolated from four HSE libraries (two GelHSEs and two FibHSEs) and two *in vivo* neonatal epidermis libraries using uniform manifold approximation and projection (UMAP) embedding. Libraries are split by sample type. Dashed lines encompass HSE-unique keratinocytes.

(G–I) Dot plots of the top differentially expressed marker genes for (G) *in vivo* clusters, (H) GelHSE clusters, and (I) FibHSE clusters.

(J–L) Percentage of total cells within each cluster split by sample type (J). A Monte Carlo permutation test shows the significance of the changes in proportion of each cell type for the FibHSEs (K) and GelHSEs (L) relative to the *in vivo* datasets. Bars represent 95% confidence interval determined via bootstrapping.

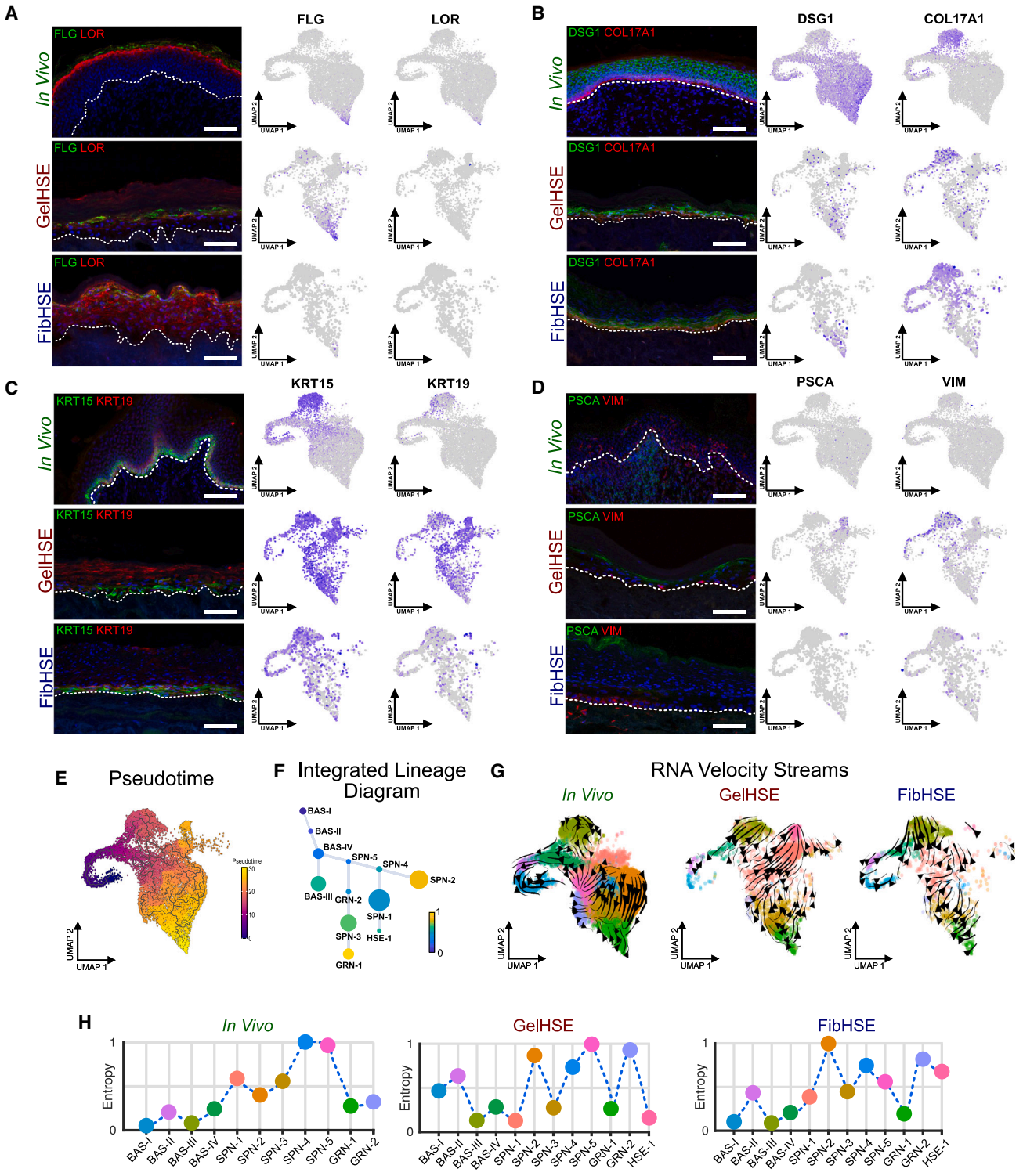

Figure 2. HSEs display altered expression patterns and lineage paths

(A–D) Immunostaining of (A) the terminal differentiation markers FLG and LOR, (B) the structural proteins DSG1 and COL17A1, (C) the BAS stem cell markers KRT15 and KRT19, and (D) the HSE-unique markers PSCA and VIM. Shown are human neonatal skin (top), day 28 GelHSEs (center), and day 28 FibHSEs (bottom). Feature plots (right) show RNA expression of the indicated markers for each sample type. Scale bars, 100 μm. Dashed lines denote the epidermal-dermal junction.

(E) Pseudotime inference of epidermal keratinocytes from the integrated datasets.

(legend continued on next page)

them to droplet-enabled scRNA-seq to resolve their individual transcriptomes (Figure S1C). We processed a total of 4,680 cells from two FibHSEs (including fibroblasts) and 4,172 cells from two GelHSEs before performing quality control analysis on individual libraries using the R package Seurat (Figure S1D). The cells from each replicate FibHSE were clustered in an unsupervised manner and tentatively annotated as keratinocytes or fibroblasts, using the marker genes *KRT14* and *KRT10* to identify keratinocytes and *TWIST2* and *COL6A1* to identify fibroblasts (Figure S2). Keratinocytes were then subset from our HSE datasets and integrated with interfollicular keratinocytes from two *in vivo* human neonatal epidermal datasets that were previously generated by our lab[27] (Figures S3A and S3B). One cluster appeared to be low-quality cells that passed our initial quality control thresholds because the number of genes detected, unique molecular identifiers (UMIs), and percent mitochondrial gene expression for each cluster appeared far lower than those of the other clusters (Figure S3C). Although it is possible that this cluster represents a genuine cell state in our HSEs, we excluded them from our downstream analyses because of their metrics and the lack of gene expression markers to identify them. Cell types were then annotated based on known marker genes from the *in vivo* dataset, which differed from the marker genes of the HSE datasets (Figures 1F–1I and S3D–S3F). Remarkably, many of the major *in vivo* cellular states were found in the *in vitro* HSEs, including the full complement of *in vivo* basal cell states. Based on our previous characterization of basal (BAS) stem cell communities,[27] BAS-I–BAS-IV represented approximately 27.3% of the *in vivo* cells, 55.6% of FibHSEs, and 22.0% of GelHSEs and were enriched for known BAS keratinocyte marker genes, including *PTTG1*, *RRM2*, *KRT15*, and *PCNA*, respectively (Figures 1J, S3G, and S3H). The ratios of BAS-I and BAS-II cycling cells remained largely similar between the *in vivo* tissue and FibHSEs, while GelHSEs had a reduction in cycling cells. BAS-III cells are enriched in both HSEs, with FibHSEs possessing over 3.5 times as many cells in this cluster than the *in vivo* tissue, whereas BAS-IV cells are depleted in the GelHSEs compared with the *in vivo* environment (Figure 1J). Intriguingly, an HSE cell state clustered separately from the *in vivo* cells and was annotated HSE-1 (Figure 1F). HSE-specific keratinocytes constituted 0.6% of FibHSEs and 9.3% of GelHSEs (Figure 1J). 10 of 12 cell type proportions were significantly changed in GelHSEs compared with the *in vivo* datasets, while only 6 of 12 were significantly different in FibHSEs (Figures 1K and 1L). Both HSEs had a higher proportion of BAS-III and HSE-I cells and a lower proportion of the spinous (SPN) cell clusters SPN-2, SPN-4, and SPN-5, and the granular (GRN) cluster GRN-2 compared with the *in vivo* state.

Despite the relatively normal histological appearance of the HSEs, there is an expansion of KRT14+ cell layers and disrupted epidermal differentiation in the GelHSE and FibHSE cultures (Figures 2A and S3I). The expanded KRT14+ cell layers do not proliferate outside of the BAS layer in contact with the basement membrane (Figure 1C), and differentiation markers such as DSG1, FLG, and LOR are still restricted from the BAS-most layer (Figures 2A and 2B). The BAS cell marker KRT15 does remain restricted to the BAS -most layer of the HSEs, whereas KRT19 shows selective expansion in GelHSEs (Figure 2C), suggesting that suprabasal KRT14+ cells are not fully functioning BAS cells and are likely to be differentiating without fully turning off the BAS cell state. The mesenchymal marker VIM, which is normally restricted to fibroblasts, melanocytes, and Langerhans cells of *in vivo* skin, shows high RNA expression in GelHSE BAS keratinocytes and VIM+ protein expression in GelHSE and FibHSE BAS keratinocytes (Figures 2D and S4), suggesting a partial EMT state. This partial EMT state is not entirely unexpected given the signals the keratinocytes are receiving from the Matrigel and culture medium, with the GelHSE showing the greatest expression of *VIM*. Cell-cell contacts and terminal differentiation are also disrupted in HSEs, with DSG1 protein no longer restricted to cell-cell contact sites, FLG protein expression turning on early in SPN cell layers, and FLG and LOR no longer restricted to the GRN layers (Figures 2A and 2B). The HSE-specific cluster HSE-1 is readily identified by one of its marker genes, *PSCA* (Figure 2D). *PSCA* encodes for a GPI-anchored membrane glycoprotein typically found in BAS cells of the prostate, the lining of the urinary tract, the mucosal epithelium of the gastrointestinal tract, and in the outermost layer of mouse fetal skin from embryonic day 15 (E15)–(E17).[31] Staining for PSCA demonstrated that these keratinocytes are exclusively localized to the outermost epidermal layers (Figures 2D and S4A) and may indicate a remnant embryonic program that is reactivated as a result of growth factors in the culture medium.

Considering the apparent uncoupling of markers from their respective cell states, we averaged the RNA expression of every cell in each cluster and calculated a Pearson correlation between the HSE and *in vivo* clusters (Figures S5A–S5E). Both *in vivo* datasets were compared with each other to establish the highest expected Pearson correlation between cell states. With respect to the HSEs, the most highly correlated clusters were the BAS cell populations. Interestingly, the majority of HSE clusters showed the highest correlation with the *in vivo* BAS-III cluster, suggesting that the BAS-III transcriptional program is not shut off during HSE differentiation. Additionally, the Pearson correlation decreases as keratinocytes differentiate, reinforcing that terminal differentiation is disrupted in HSEs. The correlation between the *in vivo* tissue and FibHSEs is higher overall than that of GelHSEs, indicating that global RNA expression in FibHSEs more accurately mimics *in vivo* human epidermis.

HSEs have altered lineage paths

Next, we examined how the HSE-specific clusters altered the inferred lineage trajectory of epidermal differentiation. We generated pseudotime and cell lineage inferences of the integrated keratinocytes using Monocle3[32] and SoptSC[33] and partially reconstructed the expected BAS-SPN-GRN keratinocyte

(F) Cell lineage diagram of keratinocytes from the integrated datasets. Edge weights denote the probability of transition to each cluster. Dot size denotes number of cells.
(G) Splicing kinetics depicted as RNA velocity streams calculated using the Python package scVelo.
(H) Quantification of Cellular Entropy (ξ) using the R package SoptSC.

differentiation trajectory (Figures 2E and 2F). BAS keratinocytes expressing *KRT15* were placed at the beginning of the trajectory, and cells expressing the terminal differentiation gene *FLG* were placed toward one of the trajectory termini (Figure 2F). Intriguingly, HSE-1 was placed at a distinct trajectory terminus away from the GRN cell states, generating a BAS-SPN-HSE differentiation trajectory (Figure 2F).

To better define the BAS-SPN-HSE differentiation trajectory, we analyzed the splicing kinetics of every cell using scVelo's dynamical modeling, to infer the future state of each cluster.[34] We subset cells from each tissue from the integrated dataset and modeled them separately while keeping their spatial relationship within the integrated UMAP space intact (Figure 2G). The *in vivo* epidermal dataset showed the expected BAS-III and BAS-IV velocity vectors pointing toward the SPN clusters and SPN velocity vectors pointing toward the GRN clusters, reconstructing the BAS-SPN-GRN differentiation trajectory (Figure 2G). While the FibHSE trajectory largely followed the aforementioned trend, many BAS and SPN velocity vectors for GelHSEs point toward the HSE-1 cluster, with an undefined flow of vectors between the SPN and GRN clusters, suggesting that terminal differentiation may be disrupted and that HSE-1 may represent an alternative differentiation trajectory terminus in the GelHSEs.

We next used SoptSC's cellular entropy estimator to infer the entropy of each cluster to determine the relative stability of each cellular state.[27] High entropy suggests a high probability that a cell will transition into another state, and low entropy indicates a low probability that a cell will transition into another state. The *in vivo* epidermal dataset shows low entropy for the BAS and GRN clusters, indicating that these are stable states, whereas the SPN clusters have high probabilities of transitioning to a new state (Figure 2H). These *in vivo* entropy values reinforce the idea that, when differentiation is initiated in the SPN state, there is momentum to reach terminal differentiation in the GRN state as an endpoint, with high energy costs to stop at any intermediate stage. For the GelHSE and FibHSE datasets, BAS-III, BAS-IV, and GRN-1 remain stable states, suggesting that these states are robust to perturbations and remain a core lineage trajectory in the HSEs (Figure 2H).

HSEs exhibit abnormal signaling associated with EMT

We sought to infer how intercellular communication is altered in the HSEs using CellChat, a bioinformatic tool that predicts intercellular communication networks using ligands, receptors, and their cofactors to represent known heteromeric molecular complexes instead of the standard one ligand/one receptor gene pair.[35] CellChat detected 18 significant signaling pathways in the *in vivo* dataset and the HSEs recapitulated 16 of the 18 pathways (Figures S5F–S5H; Table S1). However, the HSEs also showed an extended network of significant signaling pathways, with 35 in GelHSEs and 36 in FibHSEs. A subset of these pathways, such as LAMININ, CD99, CDH1, EPHB, and MPZ, show similar signaling profiles across the *in vivo* and HSE tissues, whereas the other pathways show marked differences (Figures S5F–S5H). Many of the outgoing and incoming signals in the *in vivo* dataset predominantly come from or go to the BAS-III and GRN-1 clusters, suggesting that these stable cell states have great influence over tissue function (Figure S5F). While BAS-III and GRN-1 are still signaling hubs in the GelHSE and FibHSE datasets, HSE-1-specific signaling exerts a wide influence over GelHSEs, whereas all four BAS clusters actively signal in FibHSEs, with little contribution to or from HSE-specific clusters.

Given the abnormal VIM expression in HSE BAS keratinocytes that is normally found in mesenchymal cells, we decided to explore EMT signaling in HSEs. We focused on epidermal growth factor (EGF) signaling, a well-documented inducer of EMT.[36] EGF signaling in *in vivo* epidermis mainly comes from the differentiated GRN or more differentiated SPN cell populations and signals to the BAS stem cell and early SPN populations (Figure 3A). However, sender EGF signaling is expanded to the BAS and early SPN populations in the HSEs, coinciding with the appearance of VIM+ BAS cells (Figures 2D and 3A). The HSE-1 cluster is involved in sending and receiving EGF pathway signals in GelHSEs. Interestingly, the ligands and receptors facilitating EGF signaling are substantially altered in both HSEs compared with the *in vivo* state (Figures 3B and 3C). AREG-EGFR signaling is overrepresented in both HSEs, and the *AREG* ligand is expressed in most HSE-cultured keratinocytes (Figures 3B and 3C). *EREG* and *TGFA* ligands also specifically contribute to EGF signaling in the HSEs, whereas HBEFG-EGFR signaling is reduced compared with the *in vivo* state (Figures 3B and 3C). These ligands have all been implicated in EMT induction by activation of the EGFR/ERK/nuclear factor κB (NF-κB) signaling pathway.[37–42]

Several other genes associated with EMT, such as *LAMC2* and *LGALS1*, are also expressed in HSEs (Figure 3D). LAMC2 is a regulator of the EMT phenotype, and silencing LAMC2 reverses EMT by inactivating EGF signaling,[43,44] whereas *LGALS1* promotes EMT and may be a biomarker of this process.[45,46] Both HSE cultures have high levels of *LAMC2* and *LGALS1* expression in all BAS populations and lower expression levels in more differentiated keratinocytes (Figure 3D), supporting the notion that many of the HSE BAS cells may be undergoing EMT. *VIM*, *LAMC2*, and *LGALS1* expression is higher in the Matrigel-supported GelHSEs compared with the FibHSE cultures. The epithelial cell marker *CDH1* is negatively correlated with *VIM* and shows higher expression in *VIM*- HSE keratinocytes compared with the *in vivo* state (Figure 3D), suggesting that VIM+ keratinocytes may lose contact with the underlying basement membrane, potentially explaining the small gaps we observe between BAS keratinocytes and the basement membrane in older HSE cultures (Figure 1B). Furthermore, *LAMC2* shows high-probability interactions with several integrins expressed in BAS keratinocytes, including *ITGA6*, *ITGB4*, *ITGB1*, and the cell-surface glycoprotein *CD44* (Figure 3E). *CD44* undergoes complex alternative splicing, and at least one of these isoforms is implicated in EMT.[47,48] An EMT gene module consisting of 19 genes from multiple EMT studies was used to score the EMT signature in the different samples (Table S2). GelHSEs had the highest EMT score, followed by FibHSEs and the *in vivo* dataset (Figure 3F). SLUG (SNAI2), an EMT-inducing transcription factor,[49] was present in the nuclei of keratinocytes throughout all living layers of the HSEs, while human abdominal skin had little to no observable staining, further supporting the EMT signature (Figure 3G).

Primary human keratinocytes are regularly cultured with EGF to increase the number of viable passages.[50] To define the

CellPress
OPEN ACCESS

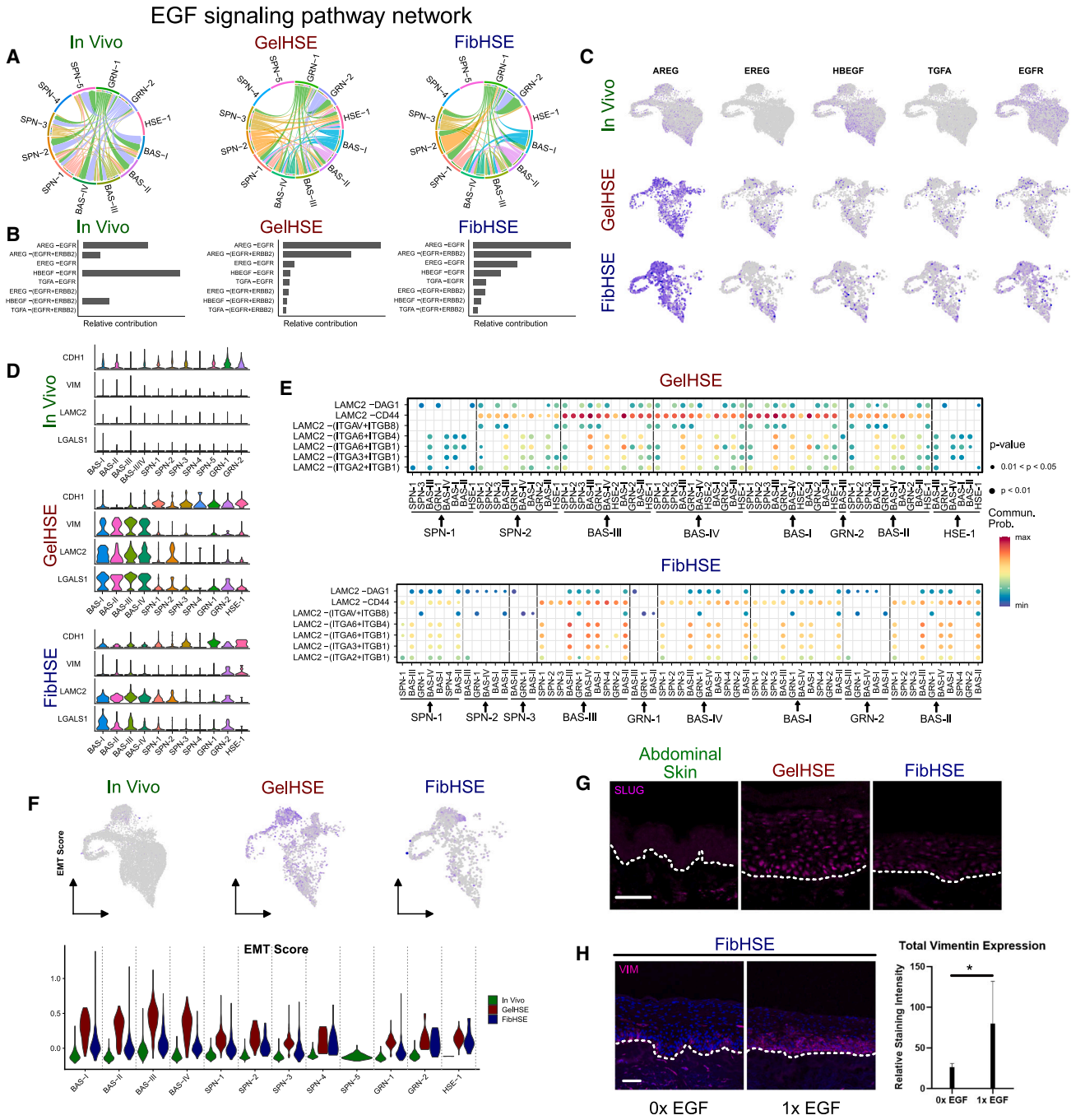

Figure 3. HSEs possess an EMT-like gene expression signature driven by EGF signaling

(A) Cell-cell communication networks predicted for the EGF signaling pathway inferred using the R package CellChat. Edge weights represent the probability of signaling between cell clusters.

(B) Relative contributions of each ligand, receptor, and cofactor group to the cell-cell communication predicted in (A).

(C) Feature plots showing the expression patterns of EGFR and each of the ligands contributing to the EGF signaling network.

(D) Violin plots of relative gene expression for positive markers (*VIM*, *LAMC2*, and *LGALS1*) and negative markers (*CDH1*) of EMT.

(E) Visualization of signaling probability scores of ligand-receptor/co-receptor pairs involving *LAMC2* for GelHSE and FibHSE datasets. *In vivo* datasets had no imputed signaling interactions involving LAMC2. Dot size represents p value.

(F) Feature plots (top) and violin plots (bottom) showing the relative EMT gene score for each cell and cluster, separated by sample type.

(G) Immunostaining of SLUG in the FibHSE, GelHSE, and *in vivo* samples. Scale bar, 100 μm.

(H) Immunostaining of VIM in FibHSEs supplemented with the indicated concentrations of EGF. Quantification of VIM staining intensity is shown on the right. n = 3 each condition. One-tailed Student's t test was used to determine significance. *p < 0.1. Scale bar, 100 μm.

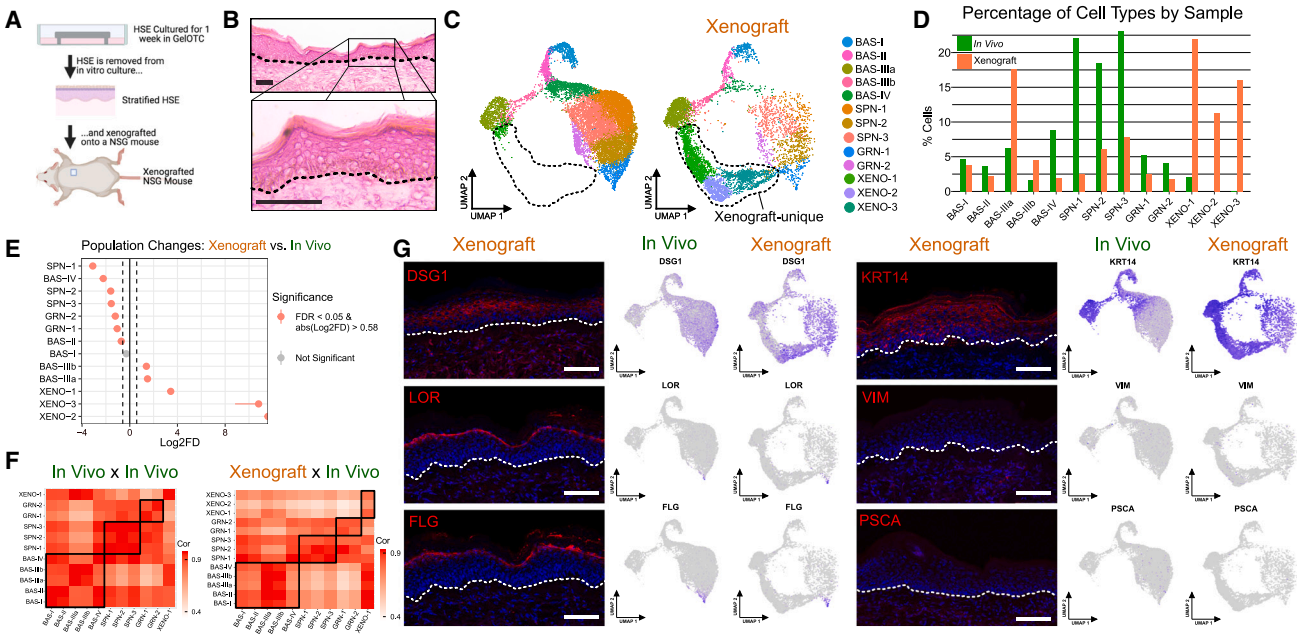

Figure 4. Xenografting rescues terminal differentiation, cell-cell adhesion, and organoid-specific programs

(A) Schematic of the strategy to xenograft HSE tissue.

(B) H&E staining of xenograft tissue. Scale bars, 100 μm. Dashed lines denote the epidermal-dermal junction.

(C) Seurat clustering of single cells isolated from pooled xenograft libraries (n = 3 samples pooled prior to sequencing) and two neonatal epidermal libraries and displayed using UMAP embedding. Libraries are split by sample type. Dashed lines encompass xenograft-unique clusters.

(D) Percentage of total cells within each cluster split by sample type.

(E) Monte Carlo permutation test showing the significance of the changes in proportion of each cell type for the xenograft relative to the *in vivo* datasets. Bars represent 95% confidence interval determined via bootstrapping.

(F) Pearson correlation of average RNA expression of each cluster compared with all other clusters between the *in vivo* datasets (left) and between the xenograft dataset and both *in vivo* datasets (right).

(G) Immunostaining of the indicated markers in HSE xenografted tissue. Feature plots show RNA expression of the indicated markers on the right. Scale bars, 100 μm. Dashed lines denote the epidermal-dermal junction.

relationship between EGF signaling and VIM+ BAS cells, FibHSEs were grown in normal growth medium that includes EGF for 1 week to induce epidermal stratification, and then the medium was replaced with new growth medium that was supplemented with either 0 × , 1 × , 2 × , or 4× EGF for an additional week (Figures 3H and S4B). The HSE growth medium uses 10 ng/mL of EGF at 1× concentration. FibHSEs were used instead of GelHSEs despite the greater GelHSE EMT score because of the inability to remove EGF from Matrigel. Removal of EGF resulted in a significant decrease in VIM expression in FibHSE keratinocytes (Figure 3H), whereas further EGF supplementation increased VIM expression (Figure S4B). These data suggest that EGF supplementation may be a major driver of EMT in HSE cultures.

Given that EMT is associated with many transcriptional changes[51,52] that may result in unique cell states that we did not detect when examining all keratinocytes, we subclustered the BAS-specific keratinocytes and found 8 distinct cell states labeled BAS-1–BAS-8 (Figure S4C). BAS-1 and BAS-8 were primarily composed of HSE-specific BAS cells, whereas BAS-4 was primarily found in the *in vivo* state (Figures S4D–S4F). The BAS-1 and BAS-8 clusters have a higher expression of VIM than the other clusters and have a higher EMT score, indicating that the keratinocytes expressing an EMT signature separate out from the other BAS populations and are primarily composed of HSE-specific BAS cells (Figures S4G and S4H).

Xenografting partially rescues HSE abnormalities

Despite using devitalized human dermis as a substrate, HSE organoid cultures have a simplified cellular composition that lack system-level aspects of normal skin, such as a fully functioning vasculature, immune system, and innervation. One way to circumvent some of these issues is to xenograft HSE cultures onto mice to more accurately mimic endogenous conditions.[7] To explore how the cellular states and transcriptional profile of HSEs were altered when xenografted onto mice, we grew three GelHSE cultures for 1 week and subsequently grafted them onto a wound bed created within the dorsal back skin of non-obese diabetic (NOD)-severe combined immunodeficiency (SCID) gamma (NSG) mice, where they remained for 24 additional days before dissecting the tissue for scRNA-seq (Figures 4A and 4B). NSG mice were chosen because of their ability to engraft skin at very high levels and perivascular infiltration of immune cells.[53] Cell suspensions from the three xenografts were pooled prior to sequencing. The xenograft dataset was aligned and annotated twice: once using the human reference genome

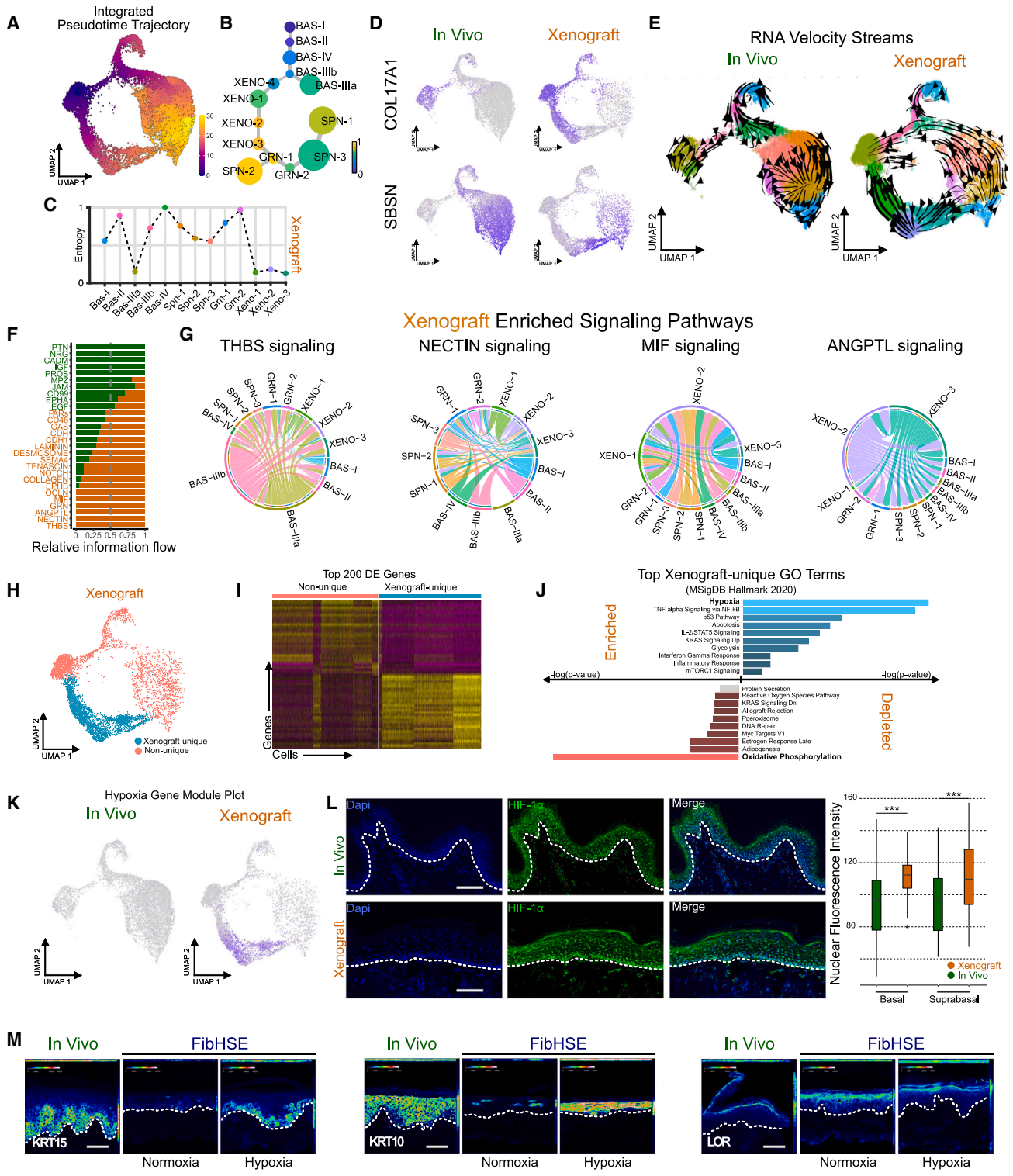

Figure 5. Hypoxia-driven transcriptional changes are observed in xenografts

(A and B) Pseudotime inference (A) and cell lineage diagram (B) of epidermal keratinocytes from the integrated *in vivo* and xenograft datasets. Edge weights denote the probability of transition to each cluster. Dot size denotes number of cells.

(C) Quantification of ξ using the R package SoptSC.

(D) Feature plots showing *SBSN* and *COL17A1*, marking differentiated and undifferentiated keratinocytes, respectively.

(E) Splicing kinetics depicted as RNA velocity streams calculated using the Python package scVelo.

(legend continued on next page)

GRCh38 and again using the mouse genome mm10. Mitochondrial gene expression and RNA features were used to identify mouse and human cells (Figures S6A and S6B). Human cells have more nuclear and mitochondrial RNA reads aligning to a human reference genome, and the same is true for mouse reads and a mouse reference genome (Figures S6C and S6D). After removing mouse cells, the dataset was compared with the *in vivo* epidermal datasets in the same manner as our HSE analyses. We excluded one cluster from our downstream analysis that appeared to be low-quality cells that passed our initial quality control thresholds because the number of genes detected and UMIs appeared to be far lower than those of the other clusters, and the percentage of mitochondrial gene expression appeared to be higher, suggesting that these were likely apoptotic cells (Figures S6E and S6F). Surprisingly, we observed three xenograft-unique clusters in the xenograft alongside the expected BAS, SPN, and GRN keratinocyte clusters (Figure 4C).

The xenograft-unique clusters were designated XENO-1–XENO-3 and collectively comprise ~49.2% of the total xenograft cells (Figure 4D). To better define the difference between the HSE and XENO cellular states, we subset and integrated the HSE-unique cells (HSE-1) with the xenograft-unique cells (XENO-1–XENO-3). The xenograft-unique keratinocytes cluster separately from the HSE-unique cells (Figure S6G), suggesting that the HSE-specific keratinocytes are unique to organoid culture and that the xenograft-unique keratinocytes are new cellular states induced after engraftment.

All of the *in vivo* cellular states are present in the xenograft HSEs (Figures 4C and 4D). However, the proportions of BAS-III and BAS-IV keratinocytes are not similar to each other, with BAS-III proportions being much higher and BAS-IV being lower in the xenograft than in the *in vivo* setting (Figures 4D and 4G), a relationship found in the GelHSE and FibHSE cultures (Figure 1H) and suggesting that the abnormal BAS cell proportions are not rescued by engraftment. The correlation between *in vivo* cell states improves in the xenograft cultures compared with the HSE cultures, and the BAS-III state is no longer expanded into the SPN and GRN states (Figure 4F vs. Figure S5). Histologically, the xenografts appear relatively normal, with some BAS keratinocytes adopting a cuboidal morphology (Figure 4B). Terminal differentiation appears to be rescued because RNA expression and immunofluorescence staining of FLG and LOR are now restricted to the GRN layer, and cell-cell contacts appear more normal, with DSG1 now localizing to cell-cell contact sites (Figure 4I), suggesting that barrier formation, which is disrupted in HSE cultures, may be rescued upon engraftment. The BAS cell states still appear to be partly disrupted, where total RNA expression for all four BAS clusters in the xenograft have the highest correlation with *in vivo* BAS-III rather than their respective cluster (Figure 4F), and KRT14 protein and RNA are still expanded into suprabasal layers (Figure 4I). Several BAS cell markers are now appropriately expressed in their corresponding cell states compared with the HSE cultures (*PTTG1* with BAS-I, *RRM2* with BAS-II, and *ASS1* and *KRT19* with BAS-III), with *COL17A1* still showing abnormal expression (Figure S6H). The two abnormal features of the HSE cultures, the partial VIM+ EMT-like state and remnant PSCA+ embryonic program, are no longer detected in the xenograft tissue (Figure 4I), suggesting that the two abnormal programs seen in the HSEs are rescued. All three XENO clusters had higher GLUT1 RNA and protein expression (Figure S7A), while XENO-3 showed an enrichment for KRT16 expression at the RNA and protein levels (Figure S7B). KRT16 is expressed in the SPN layer of human epidermis, but its localization has shifted to the GRN layer, demonstrating another change in cell state. The xenograft-unique clusters notwithstanding, the xenograft tissue more closely reflects the *in vivo* state compared with the HSE cultures with restored terminal differentiation, cell-cell adhesion, and partially restricted BAS programs.

Xenograft HSEs contain two distinct transcriptional trajectories

To characterize how the XENO clusters influence the keratinocyte differentiation trajectory, we employed pseudotime analysis overlayed onto the UMAP of the integrated *in vivo* and xenograft epithelial cells and found that xenografted keratinocytes likely follow two distinct transcriptional trajectories from BAS to GRN cells (Figures 5A and 5B). The XENO states are highly stable, along with the BAS-III state, whereas the other BAS, SPN, and GRN states are more unstable in the xenograft compared with their *in vivo* counterpart (Figure 5C). The inferred trajectory showed a progression from least differentiated to most differentiated for the xenograft-unique cell clusters, with progression from the highest *COL17A1*+ state (XENO-1) to increasing *SBSN*+ expression (XENO-3) (Figure 5D). The splicing kinetics further support two distinct differentiation trajectories, a BAS-SPN-GRN and a BAS-XENO-GRN trajectory, possessing uniform velocity streams flowing from one state to the next (Figure 5E). The abundance of the XENO cluster cells (Figure 4D) suggests that the BAS-XENO-GRN differentiation trajectory is more favored in the xenograft.

When we compare the relative information flow for the xenograft and *in vivo* datasets for each significant imputed pathway, several pathways show exclusive enrichment in the xenograft (OCLN, MIF, GRN, ANGPTL, NECTIN, and THBS) as well as the *in vivo* (PTN, NRG, CADM, insulin growth factor [IGF], and PROS) datasets (Figure 5F; Table S1). All of the pathways that

(F and G) Significant cell-cell communication networks inferred using the R package CellChat.
(H) Metaclustering of xenograft cells into xenograft-unique and non-unique cohorts.
(I) Heatmap showing the top 200 differentially expressed genes (DEGs) between the two metaclusters. The x axis represent cells from the xenograft dataset, and the y axis represents DEGs. Yellow represents relatively higher expression, while purple represents relatively low expression.
(J) Gene Ontology (GO) analysis of the top DEGs shown in (I). Blue bars indicate biological processes upregulated in xenograft-unique cells; red bars indicate biological process downregulated in xenograft-unique cells.
(K) Feature plots showing expression of a hypoxia gene module consisting of 34 hypoxia-related genes.
(L) Immunostaining of HIF1-α in human neonatal epidermis and xenograft tissue. Quantification of the nuclear HIF1-α stain is shown on the right. Significance was determined by unpaired two-tailed t test. *$p < 0.001$. Error bars represent standard error of the mean (SEM).
(M) Immunostaining for KRT15 (left), KRT10 (center), and LOR (right). Pseudocoloring represents fluorescence intensity. Scale bars, 100 μm.

are unique to xenografts are also present in at least one of the HSE cultures (Table S1). Although their functional roles within the HSE cultures are unclear, their known roles in skin biology suggest significant remodeling of the tissue and the extracellular environment. THBS signaling mainly originates in the BAS-III and XENO-1, whereas ANGPTL signaling mainly originates in XENO-2 and XENO-3 clusters (Figure 5G), and both are known to promote angiogenesis,[54,55] suggesting that the XENO clusters within the xenograft tissue may be hypoxic because of a lack of vasculature and the wound healing process from the xenograft technique. NECTIN signaling shows promiscuous signaling throughout each cluster (Figure 5G), which is to be expected given its role in cell adhesion and skin morphogenesis.[56] The MIF signaling pathway largely signals to XENO-1 and XENO-2 clusters (Figure 5G) and has been shown to be upregulated during wound healing in mice.[57]

Hypoxia partially drives transcriptome-wide changes in xenograft-unique cells

Because xenograft-unique signaling pathways indicate significant tissue remodeling, likely from the wounding process for engraftment, including enrichment for pathways that promote angiogenesis, we hypothesized that hypoxia may be a driving force behind the alternative transcriptional trajectory in the XENO clusters. This would align with the increased GLUT1 expression, a downstream target gene of the hypoxia transcription factor HIF1A, throughout all epidermal layers of the xenograft (Figure S7A). To explore this possibility, xenograft cells were metaclustered into two groups: xenograft-unique (XENO-1–XENO-3) and non-unique clusters (BAS, SPN, and GRN) (Figure 5H). The xenograft-unique and non-unique metaclusters showed unique gene expression signatures (Figure 5I), and Gene Ontology analysis was performed on the top 100 marker genes for each metacluster using the MSigDB Hallmark 2020 database (Figure 5J). The most significantly enriched term for the xenograft-unique metacluster identified hypoxia, whereas the most significantly depleted pathway was oxidative phosphorylation (Figure 5J), which has been shown to be down-regulated in response to hypoxia.[58] To explore this relationship further, we created a hypoxia gene module using Seurat's gene module function, which included a manually curated list of 34 genes that have been experimentally shown to be upregulated in response to hypoxia and/or possess a hypoxia response element in the promoter region[59–62] (Table S2). The hypoxia gene module showed enhanced gene expression in the xenograft-unique metacluster with enrichment in all XENO clusters (Figure 5K), suggesting that the xenograft tissue is under hypoxic conditions. To validate the gene expression module, we immunostained the xenografted HSE for the transcription factor HIF1A and found that nuclear HIF1A expression is significantly higher in the xenografts than in the *in vivo* tissues (Figure 5L), suggesting that hypoxia is contributing to widespread transcriptional changes in the xenografted keratinocytes. To define the relationship between hypoxia and HSE tissue architecture, we cultured FibHSEs for 14 days at 3% O_2 to mimic endogenous oxygen conditions.[63,64] Hypoxic FibHSEs expressed higher GLUT1 (Figure S7C), a downstream target gene of hypoxia and HIF1A,[65] indicating that these tissues were hypoxic under the new culture conditions. The hypoxic HSEs showed a partially repaired BAS program with KRT15 showing more uniform BAS enrichment compared with normoxic conditions (Figure 5M). The differentiation program also appeared to be partially rescued with KRT10 expression in the SPN and GRN compartments compared with the sporadic staining under normoxic conditions and LOR showing more restriction to the GRN layer. These data suggest that culturing HSEs under hypoxic conditions mimicking physiological levels instead of atmospheric oxygen levels likely improves the BAS and terminal differentiation programs of HSEs.

DISCUSSION

HSEs have long served as models of human IFE in place of murine skin.[7,18,66,67] We have shown that BAS cell heterogeneity in our organoids fully mimics *in vivo* BAS cell heterogeneity during homeostasis, with most of the differentiated states also present. However, HSE cultures exhibited signaling patterns characteristic of EMT events; contained organoid-unique cell states not found in *in vivo* neonatal epidermis, where the cells were initially isolated; and showed differentiation abnormalities. Xenografting GelHSE cultures onto NSG mice rescued many of the defects in HSE cultures but harbored xenograft-unique cell states likely driven by hypoxic conditions. These hypoxic conditions would likely last until the transplanted tissues reach homeostasis and wound repair pathways cease. For instance, the wounding keratins KRT6/KRT16 were expressed in the grafted region on days 16 and 37 in HSEs transplanted onto humans, with their expression disappearing a year after transplantation.[68] Similarly, KRT14 was expressed in all layers of the epidermis until a year post grafting, where it resumed normal BAS layer expression, suggesting that the tissue did not reach homeostasis until a year post grafting.[68] However, transplantation of HSEs onto burn patients or recent transplantation of HSEs to cure junctional epidermolysis bullosa demonstrate their clinical importance and remains the gold standard.[69]

Although BAS cell heterogeneity was intact in the HSE and xenograft tissues, the proportions of BAS-III cells were enriched and BAS-IV cells were depleted compared with the *in vivo* state. BAS-III cells typically sit atop the rete ridges *in vivo*, whereas BAS-IV cells lie at the bottom of rete ridges.[27] However, this spatial environment is lost in the HSEs because the devitalized human dermis tends to flatten out during processing (Figure 1B), suggesting that spatial positioning may be important to specify the correct proportion of BAS-III-to-BAS-IV cells. The BAS-III state also shows more stability than BAS-IV, and BAS-III transcripts are retained throughout most of the other cellular states, suggesting that the BAS-III program is not sufficiently shut down and may be the underlying cause of the differentiation defects seen in the SPN and GRN layers. Inappropriate signals from the dermis may also be the cause of the BAS defects. Although BAS cells in both HSEs expressed canonical BAS layer markers, they also expressed EMT-specific genes, such as *VIM*, *LAMC2*, and *LGALS1*. Expression of these genes was higher in the GelHSEs but still present in FibHSEs, suggesting that, while Matrigel may be enhancing EMT-like programs, replacing Matrigel with primary human dermal cells is not sufficient to induce the appropriate *in vivo* expression programs and may be due to the culture medium. Our results also suggest that HSEs may

represent a wound regeneration or development model because of their EMT features and inappropriate expression of KRT14.[51]

We identified a PSCA+ keratinocyte population, which we denoted HSE-1, unique to HSEs. Curiously, Psca expression occurs in the outermost layers of murine skin epithelium during E15–E17.[31] During this time, the outermost epithelial layer of the murine epidermis is the periderm, which forms during stratification at E11.5 and disaggregates between E16 and E17, when barrier formation occurs.[70] The periderm temporally expresses different marker genes as the epidermis differentiates, such as Krt17 during early stages and Krt6 during later stages.[70] *Psca* is upregulated in E18.5 murine epidermis of *Cyp26b1*$^{-/-}$ mice, which retains the periderm, suggesting that *Psca* may be a marker gene of the periderm at later stages. Taken together, these data suggest that primary keratinocytes from newborn epidermal tissue may retain enough plasticity to differentiate into prenatal cell types that are no longer found postnatally. Staining for KRT4, a reported periderm marker,[71] is found to be expressed in the GelHSEs and FibHSEs in all layers, but it is also detected lightly in adult abdominal skin, and therefore it is unclear whether this supports our hypothesis (Figure S8).

The presence of abnormal cell states and altered differentiation patterns in organoid cultures have been observed in a variety of tissues,[4] including skin,[9] using more conventional methods. Matrigel is used in the majority of organoid systems[4] and more than likely induces effects similar those observed here. Recent studies using scRNA-seq to characterize organoid cultures of other tissue types have also identified abnormal cell populations present in their organoid cultures. For instance, melanoma-like, neuronal-like, and muscle-like cells were found using scRNA-seq of kidney organoids,[72] which were consistent with previous observations using conventional methods in this system. scRNA-seq analysis of human intestinal and brain organoids used random forest classifiers to identify the cell types in their organoid cultures;[73,74] however, doing so precludes the possibility of classifying cells as anything other than predefined types. This is true of any supervised machine learning algorithm and can be misleading when examining cellular heterogeneity.

Despite the transcriptional and molecular differences we see in HSE organoid cultures, they still are attractive systems for investigative dermatology and are superior to 2D tissue culture of primary keratinocytes. Both HSE culture conditions form fully stratified tissues, generate the majority of *in vivo* cellular states, and largely reach homeostatic conditions after transplantation. Although xenografted HSEs are still utilizing wound repair programs 24 days post engraftment, allowing more time for the graft to heal would presumably return it to a fully homeostatic state. Potential ways to improve HSEs to more faithfully mimic *in vivo* skin could include addition of cell types such as Langerhans cells, melanocytes, endothelial cells, and other immune cells. Altering culture conditions or bioengineering 3D scaffolds may also help restrict BAS and terminal differentiating programs to their proper cellular states.

Limitations of the study

Limitations of the study include how we culture the HSE organoids. Contrary to our results, other studies do not observe any FLG and LOR expression defects when generating fibroblast-seeded HSEs. This difference may be due to the variations in culturing methods. For instance, HSEs can be completely submerged in medium for multiple days prior to raising them to an air-liquid interface to promote stratification,[75] generated with immortalized keratinocyte cell lines,[76] or seeded onto collagen layers.[77] The extent to which these changes resolve the underlying differentiation defects or give rise to new issues remains unclear. More pertinent to our study, hypoxia and angiogenesis are causally linked to wound repair, which collectively induces substantial molecular and morphological changes to tissues during repair.[78,79] While we cannot rule out wound repair as the major cause of transcriptional changes in our xenograft HSEs, hypoxia was among the most prominent differences between the xenograft HSE and the *in vivo* cell states. Because the epidermis is not directly supplied with blood, *in vivo* oxygen levels range between 0.5% and 8%.[63,64] Culturing FibHSEs under hypoxic conditions at 3% O_2 versus normoxic atmospheric conditions at 18%–20% O_2 induced molecular changes that partially resembled the xenograft HSEs, suggesting that culturing HSEs under hypoxia may be advantageous and in agreement with other findings.[60]

STAR★METHODS

Detailed methods are provided in the online version of this paper and include the following:

- KEY RESOURCES TABLE
- RESOURCE AVAILABILITY
  - Lead contact
  - Materials availability
  - Data and code availability
- EXPERIMENTAL MODEL AND SUBJECT DETAILS
  - Human tissue samples
  - Cell culture
  - Animal model details
  - Human skin equivalent organoid culture
  - Human skin equivalent xenograft model
- METHOD DETAILS
  - Preparation of devitalized dermis
  - Primary cell isolation
  - Cell sorting
  - Histology and immunohistochemistry
  - Droplet-enabled single cell RNA-sequencing and processing
  - Quality control metrics Post-Cell Ranger assessment
  - Analysis and visualization of processed sequencing data
  - Pseudotime and lineage inference
  - RNA velocity
  - Probabilistic cell-cell signaling networks
  - Cellular entropy estimation
  - EMT & hypoxia gene modules
- QUANTIFICATION AND STATISTICAL ANALYSIS

SUPPLEMENTAL INFORMATION

Supplemental information can be found online at https://doi.org/10.1016/j.celrep.2023.112511.

ACKNOWLEDGMENTS

S.X.A. is supported by NIH grant R01CA237563 and NSF grant CBET2134916. Q.N. is supported by NIH grants U01AR07315 and R01GM123731, NSF grant DMS11763272, and Simons Foundation grant 594598. A.R.S. is supported by NIH National Institute of Arthritis and Musculoskeletal and Skin Diseases (NIAMS) training grant AR080622. K.N.W. is supported by NIH National Cancer Institute (NCI) training grant CA009054. The authors wish to acknowledge the support of the Chao Family Comprehensive Cancer Center Genomics High-Throughput Facility and Optical Biology Core Shared Resource, supported by the NCI of the NIH under award no. P30CA062203 and the UCI Skin Biology Resource Center supported by NIAMS under award no. P30AR075047. We also thank Jennifer M. Atwood and the UCI Institute for Immunology Flow Cytometry Core Facility for help with cell sorting and Bryan K. Sun for comments on the manuscript.

AUTHOR CONTRIBUTIONS

S.X.A. and A.R.S. conceived the project. S.X.A. supervised the research. A.R.S. generated and analyzed scRNA-seq libraries. S.W. performed SoptSC for lineage and entropy analysis. A.R.S., S.D.N., Y.J., K.N.W., and G.E.L. performed imaging experiments. J.L. and G.L.S. performed xenograft experiments. Y.J. performed hypoxia experiments. A.R.S., Q.N., and S.X.A. analyzed and interpreted data. A.R.S. and S.X.A. wrote the manuscript. All authors analyzed and discussed the results and commented on the manuscript.

DECLARATION OF INTERESTS

The authors declare no competing interests.

Received: July 11, 2022
Revised: March 7, 2023
Accepted: April 28, 2023

REFERENCES

1. Kolarsick, P.A.J., Kolarsick, M.A., and Goodwin, C. (2011). Anatomy and physiology of the skin. J. Dermatol. Nurses Assoc. *3*, 203–213. https://doi.org/10.1097/JDN.0b013e3182274a98.
2. Ghazizadeh, S., and Taichman, L.B. (2005). Organization of stem cells and their progeny in human epidermis. J. Invest. Dermatol. *124*, 367–372. https://doi.org/10.1111/j.0022-202X.2004.23599.x.
3. Khavkin, J., and Ellis, D.A.F. (2011). Aging skin: histology, physiology, and pathology. Facial Plast. Surg. Clin. North Am. *19*, 229–234. https://doi.org/10.1016/j.fsc.2011.04.003.
4. Corrò, C., Novellasdemunt, L., and Li, V.S.W. (2020). A brief history of organoids. Am. J. Physiol. Cell Physiol. *319*, C151–C165. https://doi.org/10.1152/ajpcell.00120.2020.
5. Zomer, H.D., and Trentin, A.G. (2018). Skin wound healing in humans and mice: challenges in translational research. J. Dermatol. Sci. *90*, 3–12. https://doi.org/10.1016/j.jdermsci.2017.12.009.
6. Schmook, F.P., Meingassner, J.G., and Billich, A. (2001). Comparison of human skin or epidermis models with human and animal skin in in-vitro percutaneous absorption. Int. J. Pharm. *215*, 51–56. https://doi.org/10.1016/s0378-5173(00)00665-7.
7. Bell, E., Sher, S., Hull, B., Merrill, C., Rosen, S., Chamson, A., Asselineau, D., Dubertret, L., Coulomb, B., Lapiere, C., et al. (1983). The reconstitution of living skin. J. Invest. Dermatol. *81*, 2s–10s. https://doi.org/10.1111/1523-1747.ep12539993.
8. Bell, E., Ehrlich, H.P., Buttle, D.J., and Nakatsuji, T. (1981). Living tissue formed in vitro and accepted as skin-equivalent tissue of full thickness. Science *211*, 1052–1054. https://doi.org/10.1126/science.7008197.
9. Atwood, S.X., and Plikus, M.V. (2021). Fostering a healthy culture: biological relevance of in vitro and ex vivo skin models. Exp. Dermatol. *30*, 298–303. https://doi.org/10.1111/exd.14296.
10. Lee, J., Rabbani, C.C., Gao, H., Steinhart, M.R., Woodruff, B.M., Pflum, Z.E., Kim, A., Heller, S., Liu, Y., Shipchandler, T.Z., and Koehler, K.R. (2020). Hair-bearing human skin generated entirely from pluripotent stem cells. Nature *582*, 399–404. https://doi.org/10.1038/s41586-020-2352-3.
11. Zhang, Y., Enhejirigala, Yao, B., Li, Z., Song, W., Li, J., Zhu, D., Wang, Y., Duan, X., Yuan, X., et al. (2021). Using bioprinting and spheroid culture to create a skin model with sweat glands and hair follicles. Burns Trauma *9*, tkab013. https://doi.org/10.1093/burnst/tkab013.
12. Fauzi, M.B., Rashidbenam, Z., Bin Saim, A., and Binti Hj Idrus, R. (2020). Preliminary study of in vitro three-dimensional skin model using an ovine collagen type I sponge seeded with Co-culture skin cells: submerged versus air-liquid interface conditions. Polymers *12*, E2784. https://doi.org/10.3390/polym12122784.
13. Morrison, K.A., Weinreb, R.H., Dong, X., Toyoda, Y., Jin, J.L., Bender, R., Mukherjee, S., and Spector, J.A. (2020). Facilitated self-assembly of a prevascularized dermal/epidermal collagen scaffold. Regen. Med. *15*, 2273–2283. https://doi.org/10.2217/rme-2020-0070.
14. Stark, H.J., Baur, M., Breitkreutz, D., Mirancea, N., and Fusenig, N.E. (1999). Organotypic keratinocyte cocultures in defined medium with regular epidermal morphogenesis and differentiation. J. Invest. Dermatol. *112*, 681–691. https://doi.org/10.1046/j.1523-1747.1999.00573.x.
15. Patra, S., and Young, V. (2016). A Review of 3D printing techniques and the future in biofabrication of bioprinted tissue. Cell Biochem. Biophys. *74*, 93–98. https://doi.org/10.1007/s12013-016-0730-0.
16. Pourchet, L.J., Thepot, A., Albouy, M., Courtial, E.J., Boher, A., Blum, L.J., and Marquette, C.A. (2017). Human skin 3D bioprinting using scaffold-free approach. Adv. Healthc. Mater. *6*, 1601101. https://doi.org/10.1002/adhm.201601101.
17. Zhang, Q., Sito, L., Mao, M., He, J., Zhang, Y.S., and Zhao, X. (2018). Current advances in skin-on-a-chip models for drug testing. Microphysiol. Syst. *2*, 4. https://doi.org/10.21037/mps.2018.08.01.
18. El Ghalbzouri, A., Commandeur, S., Rietveld, M.H., Mulder, A.A., and Willemze, R. (2009). Replacement of animal-derived collagen matrix by human fibroblast-derived dermal matrix for human skin equivalent products. Biomaterials *30*, 71–78. https://doi.org/10.1016/j.biomaterials.2008.09.002.
19. Li, J., and Sen, G.L. (2015). Generation of genetically modified organotypic skin cultures using devitalized human dermis. J. Vis. Exp., e53280. https://doi.org/10.3791/53280.
20. Andreadis, S.T., Hamoen, K.E., Yarmush, M.L., and Morgan, J.R. (2001). Keratinocyte growth factor induces hyperproliferation and delays differentiation in a skin equivalent model system. FASEB J. Off. Publ. Fed. Am. Soc. Exp. Biol. *15*, 898–906. https://doi.org/10.1096/fj.00-0324com.
21. Jevtić, M., Löwa, A., Nováčková, A., Kováčik, A., Kaessmeyer, S., Erdmann, G., Vávrová, K., and Hedtrich, S. (2020). Impact of intercellular crosstalk between epidermal keratinocytes and dermal fibroblasts on skin homeostasis. Biochim. Biophys. Acta. Mol. Cell Res. *1867*, 118722. https://doi.org/10.1016/j.bbamcr.2020.118722.
22. Brancati, G., Treutlein, B., and Camp, J.G. (2020). Resolving neurodevelopmental and vision disorders using organoid single-cell multi-omics. Neuron *107*, 1000–1013. https://doi.org/10.1016/j.neuron.2020.09.001.
23. Chen, J., Lau, B.T., Andor, N., Grimes, S.M., Handy, C., Wood-Bouwens, C., and Ji, H.P. (2019). Single-cell transcriptome analysis identifies distinct cell types and niche signaling in a primary gastric organoid model. Sci. Rep. *9*, 4536. https://doi.org/10.1038/s41598-019-40809-x.
24. Serra, D., Mayr, U., Boni, A., Lukonin, I., Rempfler, M., Challet Meylan, L., Stadler, M.B., Strnad, P., Papasaikas, P., Vischi, D., et al. (2019). Self-organization and symmetry breaking in intestinal organoid development. Nature *569*, 66–72. https://doi.org/10.1038/s41586-019-1146-y.
25. van den Brink, S.C., Alemany, A., van Batenburg, V., Moris, N., Blotenburg, M., Vivié, J., Baillie-Johnson, P., Nichols, J., Sonnen, K.F., Martinez

Arias, A., and van Oudenaarden, A. (2020). Single-cell and spatial transcriptomics reveal somitogenesis in gastruloids. Nature *582*, 405–409. https://doi.org/10.1038/s41586-020-2024-3.

26. Solé-Boldo, L., Raddatz, G., Schütz, S., Mallm, J.-P., Rippe, K., Lonsdorf, A.S., Rodríguez-Paredes, M., and Lyko, F. (2020). Single-cell transcriptomes of the human skin reveal age-related loss of fibroblast priming. Commun. Biol. *3*, 1–12. https://doi.org/10.1038/s42003-020-0922-4.
27. Wang, S., Drummond, M.L., Guerrero-Juarez, C.F., Tarapore, E., MacLean, A.L., Stabell, A.R., Wu, S.C., Gutierrez, G., That, B.T., Benavente, C.A., et al. (2020). Single cell transcriptomics of human epidermis identifies basal stem cell transition states. Nat. Commun. *11*, 4239. https://doi.org/10.1038/s41467-020-18075-7.
28. Reynolds, G., Vegh, P., Fletcher, J., Poyner, E.F.M., Stephenson, E., Goh, I., Botting, R.A., Huang, N., Olabi, B., Dubois, A., et al. (2021). Developmental cell programs are co-opted in inflammatory skin disease. Science *371*, eaba6500. https://doi.org/10.1126/science.aba6500.
29. Cheng, J.B., Sedgewick, A.J., Finnegan, A.I., Harirchian, P., Lee, J., Kwon, S., Fassett, M.S., Golovato, J., Gray, M., Ghadially, R., et al. (2018). Transcriptional programming of normal and inflamed human epidermis at single-cell resolution. Cell Rep. *25*, 871–883. https://doi.org/10.1016/j.celrep.2018.09.006.
30. Maruguchi, T., Maruguchi, Y., Suzuki, S., Matsuda, K., Toda, K., and Isshiki, N. (1994). A new skin equivalent: keratinocytes proliferated and differentiated on collagen sponge containing fibroblasts. Plast. Reconstr. Surg. *93*, 537–544.
31. Ross, S., Spencer, S.D., Lasky, L.A., and Koeppen, H. (2001). Selective expression of murine prostate stem cell antigen in fetal and adult tissues and the transgenic adenocarcinoma of the mouse prostate model of prostate carcinogenesis. Am. J. Pathol. *158*, 809–816. https://doi.org/10.1016/S0002-9440(10)64028-X.
32. Cao, J., Spielmann, M., Qiu, X., Huang, X., Ibrahim, D.M., Hill, A.J., Zhang, F., Mundlos, S., Christiansen, L., Steemers, F.J., et al. (2019). The single-cell transcriptional landscape of mammalian organogenesis. Nature *566*, 496–502. https://doi.org/10.1038/s41586-019-0969-x.
33. Wang, S., Karikomi, M., MacLean, A.L., and Nie, Q. (2019). Cell lineage and communication network inference via optimization for single-cell transcriptomics. Nucleic Acids Res. *47*, e66. https://doi.org/10.1093/nar/gkz204.
34. Bergen, V., Lange, M., Peidli, S., Wolf, F.A., and Theis, F.J. (2020). Generalizing RNA velocity to transient cell states through dynamical modeling. Nat. Biotechnol. *38*, 1408–1414. https://doi.org/10.1038/s41587-020-0591-3.
35. Jin, S., Guerrero-Juarez, C.F., Zhang, L., Chang, I., Ramos, R., Kuan, C.-H., Myung, P., Plikus, M.V., and Nie, Q. (2021). Inference and analysis of cell-cell communication using CellChat. Nat. Commun. *12*, 1088. https://doi.org/10.1038/s41467-021-21246-9.
36. Kim, J., Kong, J., Chang, H., Kim, H., and Kim, A. (2016). EGF induces epithelial-mesenchymal transition through phospho-Smad2/3-Snail signaling pathway in breast cancer cells. Oncotarget *7*, 85021–85032. https://doi.org/10.18632/oncotarget.13116.
37. Aharonov, A., Shakked, A., Umansky, K.B., Savidor, A., Genzelinakh, A., Kain, D., Lendengolts, D., Revach, O.-Y., Morikawa, Y., Dong, J., et al. (2020). ERBB2 drives YAP activation and EMT-like processes during cardiac regeneration. Nat. Cell Biol. *22*, 1346–1356. https://doi.org/10.1038/s41556-020-00588-4.
38. Eapen, M.S., Sharma, P., Thompson, I.E., Lu, W., Myers, S., Hansbro, P.M., and Sohal, S.S. (2019). Heparin-binding epidermal growth factor (HB-EGF) drives EMT in patients with COPD: implications for disease pathogenesis and novel therapies. Lab. Invest. *99*, 150–157. https://doi.org/10.1038/s41374-018-0146-0.
39. Liu, S., Ye, D., Xu, D., Liao, Y., Zhang, L., Liu, L., Yu, W., Wang, Y., He, Y., Hu, J., et al. (2016). Autocrine epiregulin activates EGFR pathway for lung metastasis via EMT in salivary adenoid cystic carcinoma. Oncotarget *7*, 25251–25263. https://doi.org/10.18632/oncotarget.7940.
40. Shostak, K., Zhang, X., Hubert, P., Göktuna, S.I., Jiang, Z., Klevernic, I., Hildebrand, J., Roncarati, P., Hennuy, B., Ladang, A., et al. (2014). NF-κB-induced KIAA1199 promotes survival through EGFR signalling. Nat. Commun. *5*, 5232. https://doi.org/10.1038/ncomms6232.
41. Wang, L., Wang, L., Zhang, H., Lu, J., Zhang, Z., Wu, H., and Liang, Z. (2020). AREG mediates the epithelial-mesenchymal transition in pancreatic cancer cells via the EGFR/ERK/NF-κB signalling pathway. Oncol. Rep. *43*, 1558–1568. https://doi.org/10.3892/or.2020.7523.
42. Yu, C.-Y., Chang, W.-C., Zheng, J.-H., Hung, W.-H., and Cho, E.-C. (2018). Transforming growth factor alpha promotes tumorigenesis and regulates epithelial-mesenchymal transition modulation in colon cancer. Biochem. Biophys. Res. Commun. *506*, 901–906. https://doi.org/10.1016/j.bbrc.2018.10.137.
43. Okada, Y., Takahashi, N., Takayama, T., and Goel, A. (2021). LAMC2 promotes cancer progression and gemcitabine resistance through modulation of EMT and ATP-binding cassette transporters in pancreatic ductal adenocarcinoma. Carcinogenesis *42*, 546–556. https://doi.org/10.1093/carcin/bgab011.
44. Pei, Y.-F., Liu, J., Cheng, J., Wu, W.-D., and Liu, X.-Q. (2019). Silencing of LAMC2 reverses epithelial-mesenchymal transition and inhibits angiogenesis in cholangiocarcinoma via inactivation of the epidermal growth factor receptor signaling pathway. Am. J. Pathol. *189*, 1637–1653. https://doi.org/10.1016/j.ajpath.2019.03.012.
45. Bacigalupo, M.L., Manzi, M., Espelt, M.V., Gentilini, L.D., Compagno, D., Laderach, D.J., Wolfenstein-Todel, C., Rabinovich, G.A., and Troncoso, M.F. (2015). Galectin-1 triggers epithelial-mesenchymal transition in human hepatocellular carcinoma cells. J. Cell. Physiol. *230*, 1298–1309. https://doi.org/10.1002/jcp.24865.
46. Li, H., Zhong, A., Li, S., Meng, X., Wang, X., Xu, F., and Lai, M. (2017). The integrated pathway of TGFβ/Snail with TNFα/NFκB may facilitate the tumor-stroma interaction in the EMT process and colorectal cancer prognosis. Sci. Rep. *7*, 4915. https://doi.org/10.1038/s41598-017-05280-6.
47. Miyazaki, H., Takahashi, R.U., Prieto-Vila, M., Kawamura, Y., Kondo, S., Shirota, T., and Ochiya, T. (2018). CD44 exerts a functional role during EMT induction in cisplatin-resistant head and neck cancer cells. Oncotarget *9*, 10029–10041. https://doi.org/10.18632/oncotarget.24252.
48. Xu, H., Tian, Y., Yuan, X., Wu, H., Liu, Q., Pestell, R.G., and Wu, K. (2015). The role of CD44 in epithelial–mesenchymal transition and cancer development. OncoTargets Ther. *8*, 3783–3792. https://doi.org/10.2147/OTT.S95470.
49. Medici, D., Hay, E.D., and Olsen, B.R. (2008). Snail and slug promote epithelial-mesenchymal transition through β-catenin–T-cell factor-4-dependent expression of transforming growth factor-β3. Mol. Biol. Cell *19*, 4875–4887. https://doi.org/10.1091/mbc.E08-05-0506.
50. Rheinwald, J.G., and Green, H. (1977). Epidermal growth factor and the multiplication of cultured human epidermal keratinocytes. Nature *265*, 421–424. https://doi.org/10.1038/265421a0.
51. Haensel, D., and Dai, X. (2018). Epithelial-to-mesenchymal transition in cutaneous wound healing: where we are and where we are heading. Dev. Dyn. *247*, 473–480. https://doi.org/10.1002/dvdy.24561.
52. Jung, A.R., Jung, C.-H., Noh, J.K., Lee, Y.C., and Eun, Y.-G. (2020). Epithelial-mesenchymal transition gene signature is associated with prognosis and tumor microenvironment in head and neck squamous cell carcinoma. Sci. Rep. *10*, 3652. https://doi.org/10.1038/s41598-020-60707-x.
53. Brehm, M.A., and Shultz, L.D. (2012). Human allograft rejection in humanized mice: a historical perspective. Cell. Mol. Immunol. *9*, 225–231. https://doi.org/10.1038/cmi.2011.64.
54. Lawler, P.R., and Lawler, J. (2012). Molecular basis for the regulation of angiogenesis by thrombospondin-1 and -2. Cold Spring Harb. Perspect. Med. *2*, a006627. https://doi.org/10.1101/cshperspect.a006627.
55. Oike, Y., Yasunaga, K., and Suda, T. (2004). Angiopoietin-related/angiopoietin-like proteins regulate angiogenesis. Int. J. Hematol. *80*, 21–28. https://doi.org/10.1532/ijh97.04034.

56. Okabe, N., Ozaki-Kuroda, K., Nakanishi, H., Shimizu, K., and Takai, Y. (2004). Expression patterns of nectins and afadin during epithelial remodeling in the mouse embryo. Dev. Dyn. *230*, 174–186. https://doi.org/10.1002/dvdy.20033.

57. Gilliver, S.C., Emmerson, E., Bernhagen, J., and Hardman, M.J. (2011). MIF: a key player in cutaneous biology and wound healing. Exp. Dermatol. *20*, 1–6. https://doi.org/10.1111/j.1600-0625.2010.01194.x.

58. Rodríguez-Enríquez, S., Carreño-Fuentes, L., Gallardo-Pérez, J.C., Saavedra, E., Quezada, H., Vega, A., Marín-Hernández, A., Olín-Sandoval, V., Torres-Márquez, M.E., and Moreno-Sánchez, R. (2010). Oxidative phosphorylation is impaired by prolonged hypoxia in breast and possibly in cervix carcinoma. Int. J. Biochem. Cell Biol. *42*, 1744–1751. https://doi.org/10.1016/j.biocel.2010.07.010.

59. Kur-Piotrowska, A., Bukowska, J., Kopcewicz, M.M., Dietrich, M., Nynca, J., Slowinska, M., and Gawronska-Kozak, B. (2018). Foxn1 expression in keratinocytes is stimulated by hypoxia: further evidence of its role in skin wound healing. Sci. Rep. *8*, 5425. https://doi.org/10.1038/s41598-018-23794-5.

60. Mieremet, A., Vázquez García, A., Boiten, W., van Dijk, R., Gooris, G., Bouwstra, J.A., and El Ghalbzouri, A. (2019). Human skin equivalents cultured under hypoxia display enhanced epidermal morphogenesis and lipid barrier formation. Sci. Rep. *9*, 7811. https://doi.org/10.1038/s41598-019-44204-4.

61. Mole, D.R., Blancher, C., Copley, R.R., Pollard, P.J., Gleadle, J.M., Ragoussis, J., and Ratcliffe, P.J. (2009). Genome-wide association of hypoxia-inducible factor (HIF)-1alpha and HIF-2alpha DNA binding with expression profiling of hypoxia-inducible transcripts. J. Biol. Chem. *284*, 16767–16775. https://doi.org/10.1074/jbc.M901790200.

62. Ngo, M.A., Sinitsyna, N.N., Qin, Q., and Rice, R.H. (2007). Oxygen-Dependent differentiation of human keratinocytes. J. Invest. Dermatol. *127*, 354–361. https://doi.org/10.1038/sj.jid.5700522.

63. Evans, S.M., Schrlau, A.E., Chalian, A.A., Zhang, P., and Koch, C.J. (2006). Oxygen levels in normal and previously irradiated human skin as assessed by EF5 binding. J. Invest. Dermatol. *126*, 2596–2606. https://doi.org/10.1038/sj.jid.5700451.

64. Rezvani, H.R., Ali, N., Serrano-Sanchez, M., Dubus, P., Varon, C., Ged, C., Pain, C., Cario-André, M., Seneschal, J., Taïeb, A., et al. (2011). Loss of epidermal hypoxia-inducible factor-1α accelerates epidermal aging and affects re-epithelialization in human and mouse. J. Cell Sci. *124*, 4172–4183. https://doi.org/10.1242/jcs.082370.

65. Firth, J.D., Ebert, B.L., and Ratcliffe, P.J. (1995). Hypoxic regulation of lactate dehydrogenase A. Interaction between hypoxia-inducible factor 1 and cAMP response elements. J. Biol. Chem. *270*, 21021–21027. https://doi.org/10.1074/jbc.270.36.21021.

66. Augustin, C., Collombel, C., and Damour, O. (1997). Use of dermal equivalent and skin equivalent models for identifying phototoxic compounds in vitro. Photodermatol. Photoimmunol. Photomed. *13*, 27–36. https://doi.org/10.1111/j.1600-0781.1997.tb00105.x.

67. Gu, H., Zhu, Y., Jia, T., Li, X., Lu, Y., and Kaku, K. (2020). Development of a new eczema-like reconstructed skin equivalent for testing child atopic dermatitis-relieving cosmetics. J. Cosmet. Dermatol. *19*, 752–757. https://doi.org/10.1111/jocd.13069.

68. Ojeh, N., Akgül, B., Tomic-Canic, M., Philpott, M., and Navsaria, H. (2017). In vitro skin models to study epithelial regeneration from the hair follicle. PLoS One *12*, e0174389. https://doi.org/10.1371/journal.pone.0174389.

69. Hirsch, T., Rothoeft, T., Teig, N., Bauer, J.W., Pellegrini, G., De Rosa, L., Scaglione, D., Reichelt, J., Klausegger, A., Kneisz, D., et al. (2017). Regeneration of the entire human epidermis using transgenic stem cells. Nature *551*, 327–332. https://doi.org/10.1038/nature24487.

70. Hammond, N.L., Dixon, J., and Dixon, M.J. (2019). Periderm: life-cycle and function during orofacial and epidermal development. Semin. Cell Dev. Biol. *91*, 75–83. https://doi.org/10.1016/j.semcdb.2017.08.021.

71. Fischer, B., Metzger, M., Richardson, R., Knyphausen, P., Ramezani, T., Franzen, R., Schmelzer, E., Bloch, W., Carney, T.J., and Hammerschmidt, M. (2014). p53 and TAp63 promote keratinocyte proliferation and differentiation in breeding tubercles of the zebrafish. PLoS Genet. *10*, e1004048. https://doi.org/10.1371/journal.pgen.1004048.

72. Subramanian, A., Sidhom, E.-H., Emani, M., Vernon, K., Sahakian, N., Zhou, Y., Kost-Alimova, M., Slyper, M., Waldman, J., Dionne, D., et al. (2019). Single cell census of human kidney organoids shows reproducibility and diminished off-target cells after transplantation. Nat. Commun. *10*, 5462. https://doi.org/10.1038/s41467-019-13382-0.

73. Fujii, M., Matano, M., Toshimitsu, K., Takano, A., Mikami, Y., Nishikori, S., Sugimoto, S., and Sato, T. (2018). Human intestinal organoids maintain self-renewal capacity and cellular diversity in niche-inspired culture condition. Cell Stem Cell *23*, 787–793.e6. https://doi.org/10.1016/j.stem.2018.11.016.

74. Velasco, S., Kedaigle, A.J., Simmons, S.K., Nash, A., Rocha, M., Quadrato, G., Paulsen, B., Nguyen, L., Adiconis, X., Regev, A., et al. (2019). Individual brain organoids reproducibly form cell diversity of the human cerebral cortex. Nature *570*, 523–527. https://doi.org/10.1038/s41586-019-1289-x.

75. Roger, M., Fullard, N., Costello, L., Bradbury, S., Markiewicz, E., O'Reilly, S., Darling, N., Ritchie, P., Määttä, A., Karakesisoglou, I., et al. (2019). Bioengineering the microanatomy of human skin. J. Anat. *234*, 438–455. https://doi.org/10.1111/joa.12942.

76. Reijnders, C.M.A., van Lier, A., Roffel, S., Kramer, D., Scheper, R.J., and Gibbs, S. (2015). Development of a full-thickness human skin equivalent in vitro model derived from TERT-immortalized keratinocytes and fibroblasts. Tissue Eng. Part A *21*, 2448–2459. https://doi.org/10.1089/ten.TEA.2015.0139.

77. Mieremet, A., van Dijk, R., Boiten, W., Gooris, G., Bouwstra, J.A., and El Ghalbzouri, A. (2019). Characterization of human skin equivalents developed at body's core and surface temperatures. J. Tissue Eng. Regen. Med. *13*, 1122–1133. https://doi.org/10.1002/term.2858.

78. Botusan, I.R., Sunkari, V.G., Savu, O., Catrina, A.I., Grünler, J., Lindberg, S., Pereira, T., Ylä-Herttuala, S., Poellinger, L., Brismar, K., and Catrina, S.B. (2008). Stabilization of HIF-1alpha is critical to improve wound healing in diabetic mice. Proc. Natl. Acad. Sci. USA *105*, 19426–19431. https://doi.org/10.1073/pnas.0805230105.

79. Gurtner, G.C., Werner, S., Barrandon, Y., and Longaker, M.T. (2008). Wound repair and regeneration. Nature *453*, 314–321. https://doi.org/10.1038/nature07039.

80. Stuart, T., Butler, A., Hoffman, P., Hafemeister, C., Papalexi, E., Mauck, W.M., Hao, Y., Stoeckius, M., Smibert, P., and Satija, R. (2019). Comprehensive integration of single-cell data. Cell *177*, 1888–1902.e21. https://doi.org/10.1016/j.cell.2019.05.031.

81. Becht, E., McInnes, L., Healy, J., Dutertre, C.-A., Kwok, I.W.H., Ng, L.G., Ginhoux, F., and Newell, E.W. (2018). Dimensionality reduction for visualizing single-cell data using UMAP. Nat. Biotechnol. *37*, 38–44. https://doi.org/10.1038/nbt.4314.

82. Hao, Y., Hao, S., Andersen-Nissen, E., Mauck, W.M., Zheng, S., Butler, A., Lee, M.J., Wilk, A.J., Darby, C., Zager, M., et al. (2021). Integrated analysis of multimodal single-cell data. Cell *184*, 3573–3587.e29. https://doi.org/10.1016/j.cell.2021.04.048.

STAR★METHODS

KEY RESOURCES TABLE

REAGENT or RESOURCE	SOURCE	IDENTIFIER
Antibodies		
Chicken anti-KRT14	BioLegend	Cat#906004; RRID:AB_2616962
Rabbit anti-KI67	Abcam	Cat# ab15580; RRID:AB_443209
Rabbit anti-COL17A1	Abcepta	Cat# AP9099c; RRID:AB_10613016
Rabbit anti-KRT19	Cell Signaling Technology	Cat# 13092; RRID:AB_2722626
Mouse anti-KRT15	Santa Cruz Biotechnology	Cat# sc-47697; RRID:AB_627847
Rabbit anti-VIM	Cell Signaling Technology	Cat# 12826; RRID:AB_2798037
Mouse anti-PSCA	Santa Cruz Biotechnology	Cat# sc-80654; RRID:AB_1128761
Mouse anti-FLG	Santa Cruz Biotechnology	Cat# sc-66192; RRID:AB_1122916
Mouse anti-DSG1	Santa Cruz Biotechnology	Cat# sc-137164; RRID:AB_2093310
Mouse anti-SLUG	Santa Cruz Biotechnology	Cat# sc-166476; RRID:AB_2191897
Rabbit anti-KRT16	Thermo Fisher Scientific	Cat# PA5-99172; RRID:AB_2818105
Rabbit anti-cCASP3	Cell Signaling Technology	Cat# 9579; RRID:AB_10897512
Rabbit anti-KRT4	Proteintech	Cat# 16572-1-AP; RRID:AB_2134041
Rabbit anti-GLUT1	Proteintech	Cat# 21829-1-AP; RRID:AB_10837075
Rabbit anti-HIF1a	Proteintech	Cat# 20960-1-AP; RRID:AB_10732601
Rabbit anti-LOR	Abcam	Cat# ab85679; RRID:AB_2134912
Alexa Fluor 488	Jackson ImmunoResearch	Cat# 715-545-150; RRID:AB_2340846; Cat# 711-545-152; RRID:AB_2313584
Cy3 AffiniPure	Jackson ImmunoResearch	Cat# 711-165-152; RRID:AB_2307443; Cat# 111-165-003; RRID:AB_2338000
Biological samples		
Human skin	New York Firefighters Skin Bank	http://www.cornellsurgery.org/pro/services/burn-surgery/skin-bank.html
Chemicals, peptides, and recombinant proteins		
PEN/STREP	GIBCO	15140-122
Keratinocyte Medium (KCSFM)	Life Technologies	17005042
DMEM	GIBCO	11995
Ham's F12	Cambrex	12-615F
FBS	GIBCO	10437-028
Adenine	Sigma	A-9795
Cholera Toxin	Sigma	C-8052
Hydrocortisone	Calbiochem	3896
Insulin	Sigma	I-1882
EGF	Invitrogen	13247-051
Transferrin	Sigma	T-0665
Ciprofloxacin Hydrochloride	Serologicals	89-001-1
Matrigel	Corning	354234
Critical commercial assays		
Chromium Single Cell 3' Library & Gel Bead Kit v2	10x Genomics	PN-120237
Chromium Single Cell 3' Library & Gel Bead Kit v3	10x Genomics	PN-1000075
Chromium Single Cell A Chip Kits	10x Genomics	PN-120236
Chromium i7 Multiplex Kit	10x Genomics	PN-120262

(*Continued on next page*)

Continued

REAGENT or RESOURCE	SOURCE	IDENTIFIER
Deposited data		
Raw scRNA-seq data	This paper	GEO: GSE190695
Experimental models: Cell lines		
Primary human keratinocytes	Hospital Maternity Ward	N/A
Primary human fibroblasts	Hospital Maternity Ward	N/A
Experimental models: Organisms/strains		
NSG Mouse	Jackson Laboratory	005557
Software and algorithms		
Cell Ranger 2.1.0	10x Genomics	https://support.10xgenomics.com/single-cell-geneexpression/software/downloads/latest
Cell Ranger 3.1.0	10x Genomics	https://support.10xgenomics.com/single-cell-geneexpression/software/downloads/latest
Seurat v3	Stuart et al.[80]	https://satijalab.org/seurat/articles/archive.html
scVelo v0.2.4	Bergen et al.[34]	https://scvelo.readthedocs.io/
UMAP	Becht et al.[81]	https://github.com/lmcinnes/umap
CellChatDB, CellChat v1.5	Jin et al.[35]	https://github.com/sqjin/CellChat
Monocle3	Cao and Spielmann et al.[32]	https://cole-trapnell-lab.github.io/monocle3/papers/
SoptSC	Wang et al.[33]	https://github.com/WangShuxiong/SoptSC
Matlab	MathWorks	https://www.mathworks.com/products/new_products/release2019b.html
R	R core	https://www.r-project.org/
Python	Python Software Foundation	https://www.python.org/

RESOURCE AVAILABILITY

Lead contact

Further information and requests for resources and reagents should be directed to the lead contact, Scott Atwood (satwood@uci.edu).

Materials availability

This study did not generate new unique reagents.

Data and code availability

- The datasets generated in this study have been deposited in the GEO database under accession number GSE190695 (GEO: GSE190695). These data are publicly available as of the date of publication. Accession numbers are listed in the key resources table.
- This paper does not report original code.
- Any additional information required to reanalyze the data reported in this paper is available from the lead contact upon request.

EXPERIMENTAL MODEL AND SUBJECT DETAILS

Human tissue samples

Human clinical studies were approved by the Ethics Committee of the University of California, Irvine. All human studies were performed in strict adherence to the Institutional Review Board (IRB) guidelines of the University of California, Irvine (2009-7083). We have obtained informed consent from all participants. All available discarded and deidentified tissues were used to generate primary cells for cell and organoid culturing. Each cohort of organoids initiated on separate days used cells from a distinct subject. Human cadaver skin from the New York Firefighters Skin Bank was devitalized and used as a scaffold for organoid culturing.

Cell culture

Human primary keratinocytes and dermal fibroblasts were isolated from discarded neonatal foreskin. As such, all cells and organoids are of male origin. Primary human keratinocytes were cultured in Keratinocyte Serum Free Medium supplemented with Epidermal Growth Factor 1-53 and Bovine Pituitary Extract. Primary human fibroblasts were maintained in DMEM with 10% FBS and 1% PEN/STREP. Cells were cultured in a 5% CO_2 incubator at 37°C.

Animal model details

Female NOD scid gamma mice aged 12-14 weeks were used as the experimental model in this study. The NOD scid gamma mice were housed under standard conditions with ad libitum access to food and water. The mice were maintained in a temperature- and humidity-controlled environment with a 12-hour light/dark cycle. All maintenance, care, and experiments have been approved and abide by regulatory guidelines of the Institutional Animal Care and Use Committee of the University of California, San Diego.

Human skin equivalent organoid culture

Primary human keratinocytes were cultured in Keratinocyte Serum Free Medium supplemented with Epidermal Growth Factor 1-53 and Bovine Pituitary Extract (Life Technologies; 17005042). Generation of organotypic skin cultures were performed as described in Li and Sen, 2015. Briefly, ~500K control cells were seeded on devitalized human dermis and raised to an air/liquid interface to induce differentiation and stratification over the indicated number of days with culture changes every two days. Prior to seeding keratinocytes, either Matrigel was applied to the underside of the devitalized dermis or primary human dermal fibroblasts were centrifuged into the devitalized dermis. To evaluate the effect of oxygen levels on 3D skin cultures, FibHSEs were cultured as previously described and exposed to either normoxia (18-20% oxygen) or hypoxia (3% oxygen) at the air-liquid interface for 14 days. To measure changes from EGF supplementation, culture medium was switched to Keratinocyte Serum Free Medium supplemented with Bovine Pituitary Extract and variable concentrations of Epidermal Growth Factor 1-53 (Life Technologies; 17005042) after one week for one additional week of culturing.

Human skin equivalent xenograft model

Human neonatal epidermal keratinocytes (Thermo Fisher Scientific; C0015C) were maintained in Epilife medium (Thermo Fisher: MEPI500CA) supplemented with HGKS (Thermo Fisher: S0015). To generate skin equivalents, 10^6 cells were seeded onto devitalized human dermis and maintained in an air-liquid interface for 7 days. Stratified epithelial tissue was then grafted onto 12-14 week old female NOD scid gamma mice (Jackson Laboratory: 005557). Bandages and sutures were removed 2 weeks after surgery and healthy grafts were harvested 10 days later.

METHOD DETAILS

Preparation of devitalized dermis

Cadaver human skin was acquired from the New York Firefighters Skin Bank (New York, New York, USA). Upon arrival at UC Irvine, the skin was allowed to thaw in a biosafety cabinet. Skin was then placed into PBS supplemented with 4X Pen/Strep, shaken vigorously for 5 minutes, and transferred to PBS supplemented with 4X Pen/Strep. This step was repeated two additional times. The skin was then placed into a 37°C incubator for 2 weeks. The epidermis was removed from the dermis using sterile watchmaker forceps. The dermis was washed 3 times in PBS supplemented with 4X Pen/Strep with vigorous shaking. The dermis was then stored in PBS supplemented with 4X Pen/Strep at 4°C until needed.

Primary cell isolation

Discarded and de-identified neonatal foreskins were collected during routine circumcision from UC Irvine Medical Center (Orange, CA, US). The samples were either processed for histological staining, single cell RNA-sequencing, or primary culture. No personal information was collected for this study. For primary cell isolation, fat from discarded and de-identified neonatal foreskins were removed using forceps and scissors and incubated with dispase epidermis side up for 2 hours at 37°C. The epidermis was peeled from the dermis, cut into fine pieces, and incubated in 0.25% Trypsin-EDTA for 15 minutes at 37°C and quenched with chelated FBS. Cells were passed through a 40μm filter, centrifuged at 1500rpm for 5 minutes, and the pellet resuspended in Keratinocyte Serum Free Medium supplemented with Epidermal Growth Factor 1-53 and Bovine Pituitary Extract (Life Technologies; 17005042). Cells were either live/dead sorted using SYTOX Blue Dead Cell Stain (ThermoFisher; S34857) for single cell RNA-sequencing or incubated at 37°C for culture.

Cell sorting

Following isolation, cells were resuspended in PBS free of Ca^{2+} and Mg^{2+} and 1% BSA and stained with SYTOX Blue Dead Cell Stain (ThermoFisher; S34857). Samples were bulk sorted at 4°C on a BD FACSAria Fusion using a 100μm nozzle (20 PSI) at a flow rate of 2.0 with a maximum threshold of 3000 events/sec. Following exclusion of debris and singlet/doublet discrimination, cells were gated on viability for downstream scRNA-seq.

Histology and immunohistochemistry

Frozen tissue sections (10μm) were fixed with 4% PFA in PBS for 15 minutes. Following fixation, tissue sections were stained with Hematoxylin and Eosin following standard procedures. Sections were stained with Gill's III (Fisher Scientific; 22050203) for 5 minutes and Eosin-Y (Fisher Scientific; 22050197) for 1 minute. Tissue sections were visualized under a light microscope under 10x objective lens after mounting with Permount mounting medium (Fisher Scientific; SP15-100). For immunostaining, tissue sections were fixed with 4% PFA in PBS for 15 minutes. 10% BSA in PBS was used for blocking. Following blocking, 5% BSA and 0.1% Triton X-100 in PBS was used for permeabilization. The following antibodies were used: chicken anti-KRT14 (1:500; BioLegend; SIG-3476), rabbit anti-KI67 (1:500; Abcam; ab15580), rabbit anti-COL17A1 (1:100; One World Labs; ap9099c), rabbit anti-KRT19 (1:250; Cell signaling; 13092), mouse anti-KRT15 (1:500; Santa Cruz; sc-47697), rabbit anti-VIM (1:500; Cell Signaling; D21H3), mouse anti-PSCA (1:500; Santa Cruz; sc-80654), mouse anti-FLG (1:500; Santa Cruz; sc-66192), mouse anti-DSG1 (1:500; Santa Cruz; sc-137164), mouse anti-SLUG (1:500; Santa Cruz; sc-166476), rabbit anti-KRT16 (1:500; Invitrogen; PA5-99172), rabbit anti-cCASP3 (1:500; Cell Signaling; 9579T), rabbit anti-KRT4 (1:500; Fisher Scientific; 16572-1-AP), rabbit anti-GLUT1 (1:500; Proteintech; 218291AP), rabbit anti-HIF1a (1:500; Proteintech; 501733175), and rabbit anti-LOR (1:500; Abcam; ab85679). Secondary antibodies included Alexa Fluor 488 (1:500; Jackson ImmunoResearch; 715-545-150, 711-545-152) and Cy3 AffiniPure (1:500; Jackson ImmunoResearch; 711-165-152, 111-165-003). Slides were mounted with Prolong Diamond Antifade Mountant containing DAPI (Molecular Probes; P36962). Confocal images were acquired at room temperature on a Zeiss LSM700 laser scanning microscope with Plan-Apochromat 20x objective or 40x and 63x oil immersion objectives. Images were arranged with ImageJ, Affinity Photo, and Affinity Designer.

Droplet-enabled single cell RNA-sequencing and processing

Cell counting, suspension, GEM generation, barcoding, post GEM-RT cleanup, cDNA amplification, library preparation, quality control, and sequencing was performed at the Genomics High Throughput Sequencing Facility at the University of California, Irvine. Transcripts were mapped to the human reference genome (GRCh38) using Cell Ranger Version 3.1.0.

Quality control metrics Post-Cell Ranger assessment

For downstream analyses, we kept cells which met the following filtering criteria per biological replicate per condition: >200 and <5000 genes/cell, and <10% mitochondrial gene expression. Genes that were expressed in less than 3 cells were excluded. Data were normalized with a scale factor of 10,000. Following downstream integration and clustering, one cluster in the In Vivo, GelHSE, and FibHSE integrated dataset, HSE-2, had an average of 469 unique genes expressed and 805 UMIs indicating that these are low quality cells. Similarly, one cluster in the In Vivo and Xenograft integrated dataset, XENO-4, had an average of 807 unique genes expressed and 1881 UMIs. This cluster was also excluded from downstream analysis.

Analysis and visualization of processed sequencing data

Seurat[82] and SoptSC[33] were implemented for analysis of scRNA-seq data in this study. Seurat was performed in R (version 4.2.1) and was applied to all the datasets in this study. To select highly variable genes (HVGs) for initial clustering of cells, we performed Principal Component Analysis on the scaled data for all genes included in the previous step. For clustering, we used the function FindClusters that implements Shared Nearest Neighbor modularity optimization-based clustering algorithm on 20 PC components. A nonlinear dimensionality reduction method, UMAP, was applied to the scaled matrix for visualization of cells in two-dimensional space using 20 PC components. The marker genes for every cluster compared with all remaining cells were identified using the FindAllMarkers function. For each cluster, genes were selected such that they were expressed in at least 25% of cells with at least 0.25-fold difference.

Pseudotime and lineage inference

Pseudotime and lineage analysis were performed using Monocle3 and SoptSC, respectively. Briefly, pseudotime was calculated as the shortest path distance between cells and root cell on the cell-to-cell graph constructed based on the similarity matrix. Root cell was identified by the user in Monocle3. Visualization of the cell trajectories was obtained using UMAP. Cell states were visualized using abstract lineage trees. Lineage trees are obtained by computing the minimum spanning tree of the cluster-to-cluster graph based on the shortest path distance between cells. Pseudotime was projected on the lineage tree such that the order of each state (cluster) was defined as the average distances between cells within the state and the root cell. The root cell for DPT was selected from the BAS-I cluster.

RNA velocity

RNA velocity was estimated based on the spliced and unspliced transcript reads from the single-cell data. We followed the standard process of the velocyto pipeline to generate the spliced and unspliced matrices by applying velocyto.py to the data from the Cell Ranger output (outs) folder. Only interfollicular epidermal keratinocytes and the HSE unique keratinocytes were used to calculate velocity vectors. RNA velocity was estimated using the python package scVelo and then the velocity fields were projected onto the UMAP space produced by Seurat. Default settings were used for the rest of the parameters.

Probabilistic cell-cell signaling networks

The R package CellChat was used to infer, analyze, and visualize cell-cell communication from our scRNA-seq data. The preprocessed and normalized data from the Seurat objects were used as input for creating the CellChat objects. All known molecular interactions, including the core interaction between ligands and receptors with multi-subunit structure and additional modulation by cofactors, are integrated into a mass action-based model to quantify the communication probability between a given ligand and its cognate receptor. The signaling communication probability between two cell groups is modeled by considering the proportion of cells in each group across all sequenced cells. An option is provided for removing the potential artifact of population size when inferring cell-cell communication.

Cellular entropy estimation

Cellular Entropy (ξ) measures the likelihood that a cell will transition to a new state (i.e., from one cluster to another). Lower entropy values indicate that the cell remains in a steady state, while higher entropy values imply the cell inherits multiple state properties and is more likely to transition to a new state. Via the non-negative matrix factorization step in SoptSC, the probability of each cell assigned to each cluster is calculated.

EMT & hypoxia gene modules

Gene modules were created using Seurat's AddModuleScore function and visualized using the FeaturePlot function. The genes used in each gene module were manually curated from literature with a focus on gene expression studies involving keratinocytes. All of the genes used in both gene modules along with the citations for the specific study that characterizes the gene's role in EMT and hypoxia can be found in Table S2.

QUANTIFICATION AND STATISTICAL ANALYSIS

Data are presented as the mean ± standard error of mean (SEM), as indicated. The sample sizes in each plot have been listed in the Results section and Figure Legends where appropriate. For differential gene expression analysis between cell clusters and data represented as violin plots, two-tailed Wilcoxon rank sum test was performed using R (https://www.r-project.org/). For comparison of cell population changes, a permutation test was performed using R. A significance threshold of $p < 0.01$ was used for defining marker genes of each cell cluster. For data presented in box or bar plots, an unpaired two-tailed Student's t-test was used when comparing two groups and a one-way ANOVA followed by Tukey's HSD was used when comparing three or more groups.